



Activation of persulfate on fluorinated carbon: Role of semi-ionic C-F in inducing mechanism transition from radical to electron-transfer nonradical pathway

Feng Ye^a, Yinmei Su^a, Ruipeng Li^a, Wei Sun^{a,*}, Mengjie Pu^a, Cao Yang^a, Wenchao Yang^b, Haiming Huang^a, Qichun Zhang^c, Jonathan W.C. Wong^{a,d,**}

^a Research Center for Eco-environmental Engineering, Dongguan University of Technology, Dongguan 523830, PR China

^b Guangling College and School of Plant Protection, Yangzhou University, Yangzhou, PR China

^c Center of Super-Diamond and Advanced Films (COSDAF), City University of Hongkong, 999077, Hong Kong Special Administrative Region

^d Institute of Bioresource and Agriculture, Hong Kong Baptist University, Hong Kong Special Administrative Region

ARTICLE INFO

Keywords:

Persulfate
Fluorinated carbon
Electron transfer
Positively charged carbon
Semi-ionic C-F

ABSTRACT

Carbon-driven nonradical persulfate activation exhibits compelling advantages due to its good reactivity in complex aquatic surroundings. However, uncertainties still exist in the construction of nonradical-oriented activation systems and the role of positively charged carbon is ambiguous because of intricate carbon structure. In this regard, this study found that F-doping strategy not only improved the catalytic activity of carbon material, but also switched free radical persulfate (PS)-activated process into the electron-transfer-based nonradical process. The CF-1.0 achieved the promising performance in degrading bisphenol A (BPA) with a removal rate of 99.5% within 60 min, where the percentage of electron transfer contribution was up to 73.27%. Based on the Bader charge analysis in density functional theory (DFT) calculation, the “electron-loss” induced catalytic mechanism was proposed. Stimulated by the incorporation of F atom that can create the electron-deficient carbon layer, the electron-rich BPA tended to transfer electrons to carbon-activated persulfate complex ($\text{C-S}_2\text{O}_8^{2-*}$), in an effort to balance the electron loss in the carbonaceous matrix, thereby realizing the oxidative degradation of pollutant. Quantitative structure-activity relationships (QSARs) indicated that semi-ionic C-F, C-OH, and structural defects could function as electron transfer channel, $\text{SO}_4^{\cdot-}/^{\cdot}\text{OH}$, and $^1\text{O}_2$ formation sites, respectively. In addition, the catalytic behaviors towards periodate (PI) were also investigated in detail. Overall, this research develops nonradical reaction-targeted fluorinated carbocatalyst for persulfate activation and deepens the understanding of positively charged carbon in electron-transfer regime.

1. Introduction

With the advance of society, the plastic industry has become booming, and the global production of plastic was up to 367 million tons in 2020 [1]. Bisphenol A (BPA) is a widely-used industrial raw material for producing polycarbonate and epoxy resin [2]. Inevitably, the release of BPA from the aging and decomposition of plastic to aquatic surroundings will cause environmental contamination [3]. Excessive exposure to BPA may lead to metabolic disorders for human beings and other organisms, because BPA is a typical endocrine disruptor [4]. Multifarious strategies have been developed to remove BPA, such as

adsorption, electrocoagulation, photocatalytic oxidation, membrane separation, and so on [5–7]. Among them, persulfate-based advanced oxidation processes (PS-AOPs) is appealing for wastewater remediation benefiting from the generation of highly reactive oxygen species, such as sulfate radical ($\text{SO}_4^{\cdot-}$, 2.5–3.1 V), hydroxyl radical ($^{\cdot}\text{OH}$, 1.9–2.7 V), and singlet oxygen ($^1\text{O}_2$, 1.40 V) [8,9]. Persulfate is comprised of peroxydisulfate (PDS, $\text{S}_2\text{O}_8^{2-}$) and peroxymonosulfate (PMS, HSO_5^-), where PDS has gained more attention by virtue of its higher oxidation potential (2.01 V) and better stability [10].

In comparison to most transition-metal oxides-driven persulfate activation that produces radicals, carbonaceous materials (reduced

* Corresponding author.

** Corresponding author at: Research Center for Eco-environmental Engineering, Dongguan University of Technology, Dongguan 523830, PR China.

E-mail addresses: xunw@dgut.edu.cn (W. Sun), jwcwong@hkbu.edu.hk (J.W.C. Wong).

<https://doi.org/10.1016/j.apcatb.2023.122992>

Received 24 January 2023; Received in revised form 6 June 2023; Accepted 11 June 2023

Available online 12 June 2023

0926-3373/© 2023 Elsevier B.V. All rights reserved.

graphene, activated carbon, biochar, and carbon nanotubes) can mediate the nonradical activation of persulfate, including singlet oxygen and electron transfer, which is more resistant to the interference of water matrices without metal-ion leaching [11,12]. Furthermore, the nonradical oxidation shows high selectivity to attack electron-rich pollutants, being applicable to the oxidation of phenols and amines [13]. However, the pristine carbon materials exhibit marginal reactivity in activating persulfate due to the chemical inertness [14]. Nitrogen doping is an effective and plausible way to improve the catalytic activity of carbon material by manipulating the electronic structure and surface chemical properties in the carbonaceous skeleton [15,16]. Particularly, the incorporated nitrogen atom with the larger electronegativity compared to carbon (χ_N : 3.04 > χ_C : 2.55) can stimulate the electron transfer from adjacent C to N atoms and result in positively charged carbon, which manifests strong coupling effect with peroxide O-O bond in $S_2O_8^{2-}$, as a result enhancing the oxidative potential of carbon-activated persulfate complex ($C-S_2O_8^{2-*}$) [17]. Then, the formed $C-S_2O_8^{2-*}$ attracts electrons from contaminants to initiate the nonradical oxidation via electron-transfer.

Occasionally, with a different scenario, the N-containing groups (graphitic N and pyrrolic N) can act as the catalytic sites for persulfate activation toward $SO_4^{\cdot-}/^{\cdot}OH$ production. In this case, the radical pathway is predominant rather than electron-transfer process [18,19]. Thus, randomness and uncertainty still exist for N-doping strategy to construct the nonradical oxidation system. Although the co-doping of nitrogen and boron into π -conjugated carbon network switches the radical persulfate activation to electron-transfer-dominated nonradical process, the neutralization effect between electron-rich N and electron-deficient B atom may weaken the catalysis [20,21]. In addition, the role of positively charged carbon is vague, because the N-functionalities (graphitic N, pyridinic N, and pyrrolic N) also can mediate the electron transfer from pollutant to persulfate [15,22,23]. From the point of view, the N-doped carbon matrix is not the ideal platform to elucidate the function of positively charged carbon. Hence, more efforts should be taken to develop the nonradical reaction-targeted carbocatalysts and identify the active sites in persulfate activation.

In this regard, fluorine (F) is supposed to be the most perfect candidate for heteroatom dopants (N, O, S, B, P, Se) [4,24–26]. Thanks to the largest electronegativity of F (χ_F = 4.00), its incorporation into the sp^2 -hybridized carbon framework tends to polarize the adjacent carbon atom and results in the highest positively charged carbon, which can strengthen the interaction between carbon and persulfate, exhibiting great potential for nonradical oxidation [27,28]. Moreover, along with F doping, the local symmetry and geometry of carbon network may alter owing to the atomic size difference between C and F (F: 0.64 Å vs C: 0.77 Å), facilitating the formation of structural defects (zigzag edges, armchair edges, and vacancies). The structure defects were considered as the primary active site for 1O_2 generation in persulfate activation [29]. Especially, the fluorinated carbon materials contain three kinds of C-F configurations, including ionic, semi-ionic, and covalent bonds, where the ionic and semi-ionic C-F possess excellent catalytic activity in the fields of carbon dioxide, nitrogen, and oxygen electroreduction [3, 30]. However, the F-doped carbonaceous persulfate activator has not been reported up to now, and the activation mechanism of persulfate on fluorinated carbon is also unknown. Regarding the synthetic strategies to prepare F-embedded carbon, previous scheme was time-consuming and dangerous using toxic fluorine gas (F_2), while plasma dissociation synthesis with CF_4 as fluorine precursor is uneconomical on account of its high price [31]. Therefore, it is highly desirable to exploit a simple synthetic method to prepare F-doped carbon and investigate the catalytic effect in persulfate activation.

Herein, for the sake of nonradical-oriented persulfate activation system, F doping strategy is utilized to fabricate the carbonaceous persulfate activator. The two-step synthesis was involved: hydrothermal treatment with glucose/polytetrafluoroethylene dispersion and the subsequent high temperature carbonization. The as-prepared

carbocatalysts were characterized by SEM, TEM, XRD, FT-IR, Raman, BET, and XPS. BPA was selected as the model contaminant (Text S1). Quenching experiments, EPR, electrochemical tests, XPS, and Raman spectroscopy were employed to identify the active sites and carbocatalytic mechanism. Furthermore, quantitative structure-activity relationships (QSARs) were determined to reveal the respective reactive sites behind radical and nonradical pathways. The activation mechanism was further investigated by density functional theory (DFT) calculation. Degradation parameters, including catalyst dosage, PS dosage, pH, coexisting inorganic ions, and various oxidants, were examined. Also, the degradation pathways and the catalytic behaviors towards periodate (PI) were investigated in detail.

2. Materials and methods

2.1. Reagents and chemicals

All reagents and chemicals were analytical grade and used without further purification (Text S2).

2.2. Preparation of carbocatalysts (CF-X)

Scheme 1 exhibited the synthetic routes of F-doped and pristine carbon. Briefly, 4 g glucose and X mL ($X = 0.8, 2.0, 4.0, \text{ and } 6.0$) polytetrafluoroethylene (PTFE) dispersion (60 wt%) were mixed into 10 mL ethanol, in which 1 mL PTFE dispersion contained 1 g pure PTFE approximately. The mixture was added a certain amount of deionized water to 70 mL and homogeneously mixed by vigorous agitation. Afterward, the obtained suspension was transferred to a 100 mL Teflon-lined autoclave, and heated to 180 °C for 10 h via hydrothermal method. Upon cooling to room temperature, the crude product was extracted, washed, and dried to get the glucose-derived carbon spheres@PTFE complex. The subsequent carbonization process was implemented at 800 °C for 2 h with the heating rate of 5 °C min^{-1} under N_2 atmosphere. The resulting crude carbon was crushed into fine particles, rinsed with deionized water and ethanol, and then dried at 60 °C overnight to obtain the desired fluorine-doped (F-doped) carbocatalysts (CF-X). For comparison, the F-free carbon material CF-0 was synthesized through a similar procedure without adding PTFE. According to the mass ratio of added PTFE to glucose, these samples were designated as CF-0.2, CF-0.5, CF-1.0, and CF-1.5, respectively.

2.3. Batch experiments

The degradation experiments were shown in Text S3.

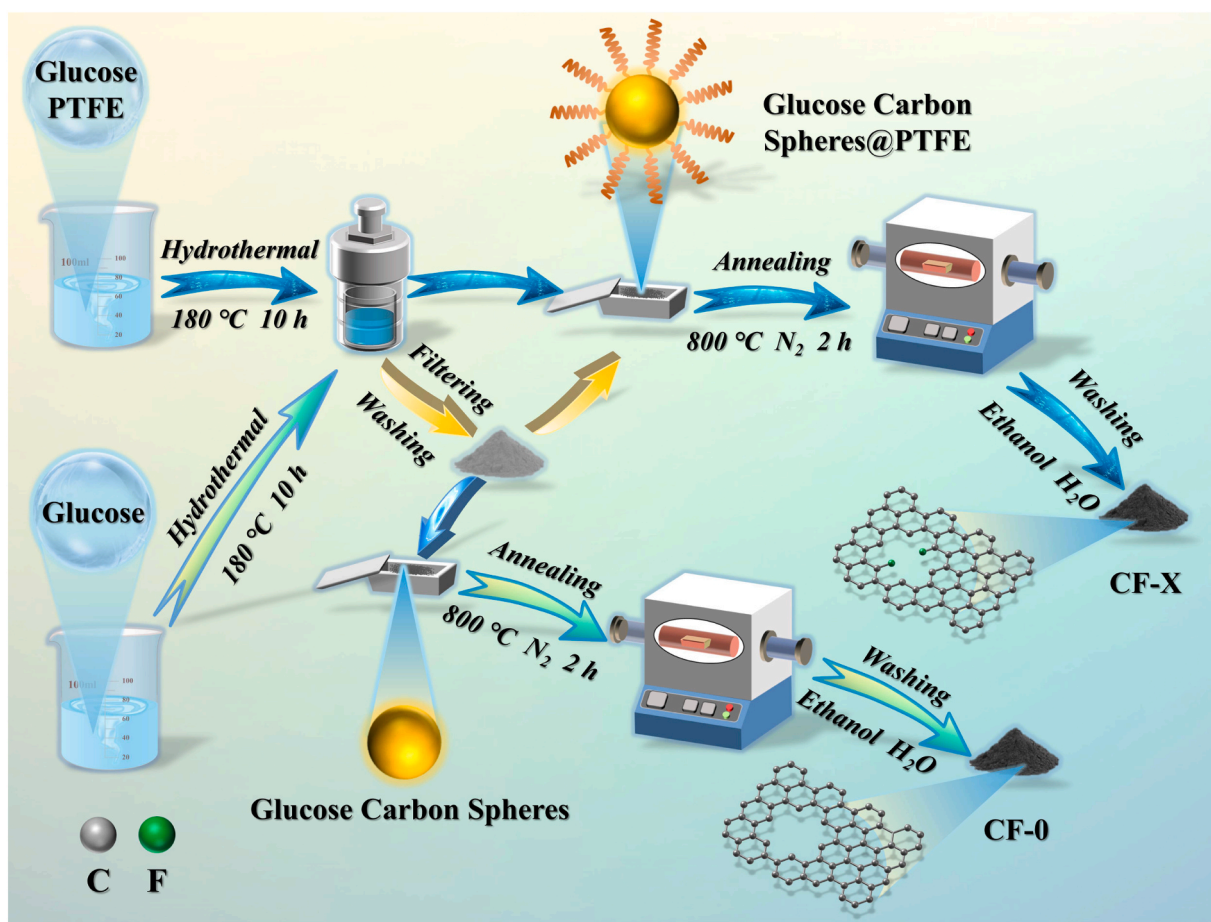
2.4. Characterization, analytical methods, and density functional theory calculation

The characterization, analytical methods, and density functional theory (DFT) calculation were shown in Supporting Information (Text S4–S5).

3. Results and discussion

3.1. Characterization of carbocatalysts

The morphology of CF-X was observed by scanning electron microscopy (SEM) and transmission electron microscopy (TEM). The pristine carbon CF-0 showed a spherical structure with smooth surface (Fig. 1a). In contrast, the morphology underwent a dramatic change with F doping, exhibiting very rough and wrinkled structure (Fig. 1b–e). This was probably due to that the incorporation of F atom into sp^2 -hybridized graphitic carbon skeleton created the structural defects. As depicted in Fig. 1f, the TEM image presented the distinct lattice fringe with 0.34 nm layer spacing, which belonged to the (002) plane of graphite, implying



Scheme 1. Schematic synthesis of carbocatalysts CF-X.

the graphitic structure of CF-1.0 [23]. From the energy dispersive spectrum of CF-1.0 in Fig. 1g, one concluded that the three elements C, O, and F were uniformly distributed on the surface of carbon materials.

The X-ray diffraction (XRD) patterns of as-derived carbon materials were shown in Fig. 2a. All catalysts displayed two diffraction peaks centered at 24° and 44° , corresponding to the (002) and (100) planes of amorphous and crystalline carbon, respectively. These results revealed that F doping did not change the crystalline structure of carbon material. Fig. 2b showed the Fourier transform infrared spectroscopy (FT-IR) of carbocatalysts. All samples exhibited strong absorption peaks at 1623 cm^{-1} and 3435 cm^{-1} , which were indexed as the stretching vibration of C=O and -OH group, respectively. As co-heating with PTFE, a new diffraction peak appeared at 1130 cm^{-1} , standing for the C-F bond [32]. In Raman spectroscopy, the D-band at 1350 cm^{-1} and G-band at 1580 cm^{-1} referred to the disordered and graphitized carbon, respectively [16]. Generally, the intensity ratio of D-band to G-band (I_D/I_G) was used to quantify the defective degree of carbonaceous materials. Considering the much higher electronegativity of F than C ($\chi_F: 4.00$ vs $\chi_C: 2.55$) as well as different atom radii (F: 0.64 \AA vs C: 0.77 \AA), embedding F can regulate the electronic cloud structure of carbon atoms far beyond several bonds (C-C-F) [28]. As a consequence, that will alter the C-C bond length in local region and increase the asymmetry of carbon network, facilitating the formation of structural defects. As predicted, F-doped carbons exhibited higher defective degrees than that of pristine carbon, and the I_D/I_G values were ordered as CF-1.0 (0.9880) > CF-0.5 (0.9807) > CF-0.2 (0.9725) > CF-0 (0.9514) (Fig. 2c). Albeit a lower F content for CF-1.5 (0.80%) relative to CF-1.0 (0.87%) but a larger I_D/I_G of 0.9956, at this time, the porous structure formation might account for the enhancement of defect degree, supported by $0.34\text{ cm}^3\text{ g}^{-1}$ for CF-1.5 > $0.32\text{ cm}^3\text{ g}^{-1}$ for CF-1.0.

The specific surface area (S_{BET}), pore volume, and pore diameter were characterized by N_2 adsorption-desorption isotherms. Related parameters were summarized in Table S1. As shown in Fig. 2d, the type IV isotherm with distinct H2 hysteresis loop demonstrated the microporous and mesoporous structure, being consistent with the average pore size distribution within 1.90–3.16 nm (Fig. S1) [33]. Noticeably, upon F atom doping, the S_{BET} of CF-0.2 ($349.41\text{ m}^2\text{ g}^{-1}$) was increased by 8-folds compared with CF-0 ($43.27\text{ m}^2\text{ g}^{-1}$). This is because the forming structure defect induced by F doping altered the morphology from smoothly spherical to wrinkled irregular shape (Seen SEM in Fig. 1a-b), in return enhancing the S_{BET} . As the other interpretation, the gas (F_2 , HF, tetrafluoroethylene, etc.) volatilization from PTFE decomposition passed through the carbon layer and left the numerous “escaping” tunnels, resulting in the formation of the porous structure and the increased S_{BET} . Analogously, the S_{BET} was positively correlated to the amount of PTFE from $349.41\text{ m}^2\text{ g}^{-1}$ to $528.06\text{ m}^2\text{ g}^{-1}$.

The surface chemical states of the prepared carbocatalysts were studied by X-ray photoelectron spectroscopy (XPS). Table S2 listed the relative atomic percentages of C, O, and F. A positive correlation between PTFE and F-doping content could be observed, corresponding to 0.20%, 0.46%, and 0.87% for CF-0.2, CF-0.5, and CF-1.0, respectively. Noting that, as the enhanced glucose/PTFE ratio to 1.5, the F doping amount of 0.80% was approximately equivalent to that of CF-1.0 and there was no further increase (Fig. S2). Such result was possibly due to that the incorporation of strongly electron-withdrawing F will lower the charge density of carbon matrix, leading to the resistant to the follow-up F atom doping via radical chain reaction. Commonly, the fluorinated carbons contained three kinds of C-F configurations, such as ionic, semi-ionic, and covalent bonds. However, as illustrated in the high-resolution F 1s spectrum, the F species was merely deconvoluted into semi-ionic C-

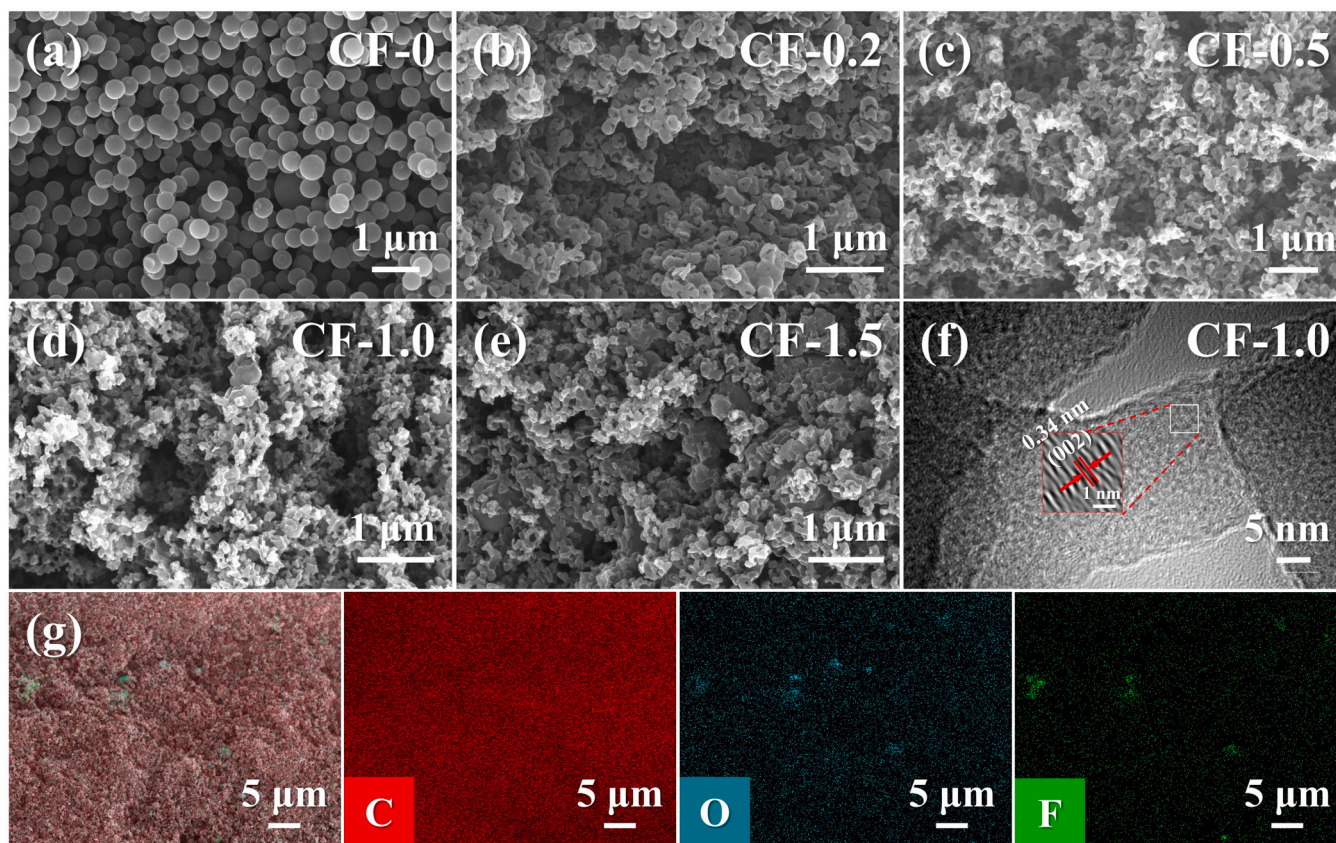


Fig. 1. SEM images of CF-0 (a), CF-0.2 (b), CF-0.5 (c), CF-1.0 (d), and CF-1.5 (e); HR-TEM image of CF-1.0 (f); EDS elemental mappings of C, O, and F for CF-1.0 (g).

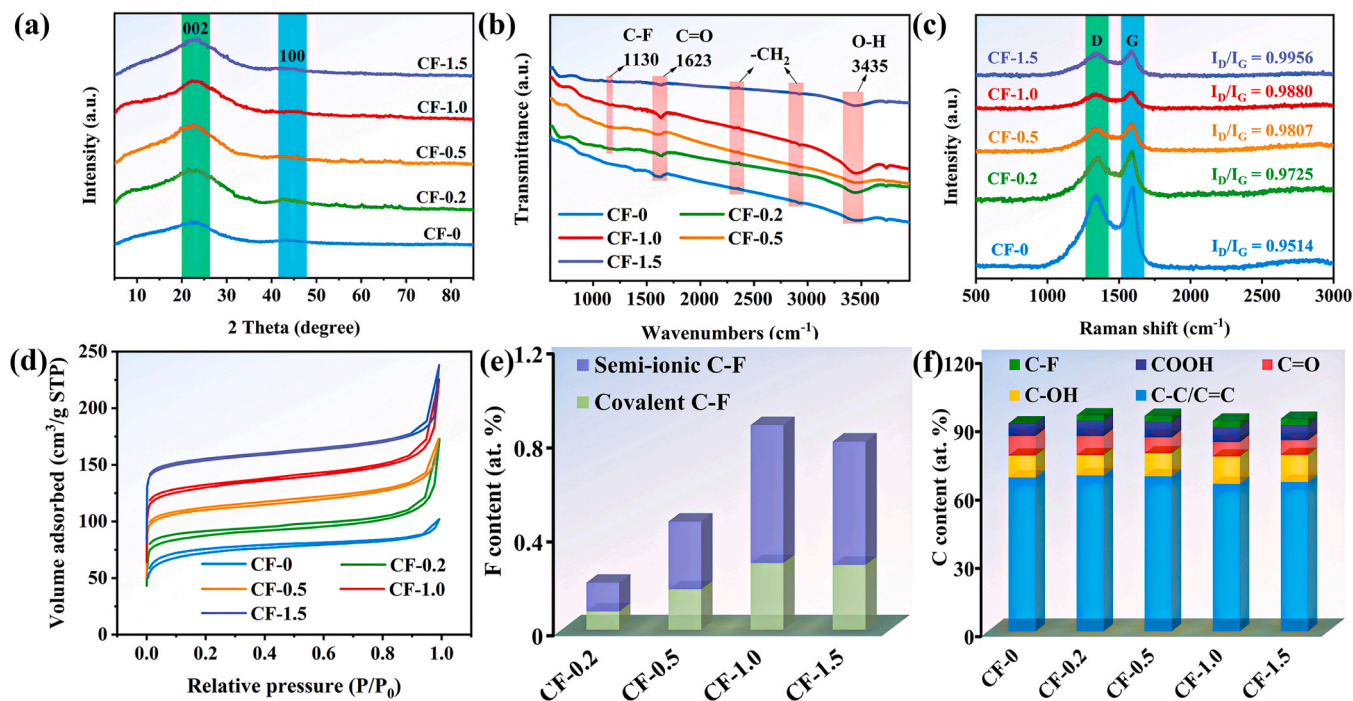


Fig. 2. XRD patterns (a), FT-IR spectra (b), Raman spectra (c), and N₂ adsorption-desorption isotherms (d) of as-synthesized carbocatalysts; Content of semi-ionic and covalent C-F (e); Content of C species (f).

F at 688.16 eV and covalent C-F at 689.50 eV (Fig. 2e and Fig. S3) [34, 35]. The previous research validated that the semi-ionic C-F possesses higher catalytic activity in contrast to covalent C-F (Text S6 and Fig. S4

[31]. As for CF-1.0, the relative ratio of semi-ionic to covalent bond is maximum about 2.07, signifying the superior catalytic activity (Table S3). The C 1s spectrum was divided into four components:

C-C/C=C (284.80 eV), C-OH (285.98 eV), C=O (286.98 eV), O=C-O (288.63 eV), and C-F (290.29 eV) (Fig. 2f, Fig. S5, and Table S4).

3.2. PS activation performance

Bisphenol A (BPA) was employed to evaluate the catalytic activity of as-prepared carbons by coupling with PS. Prior to catalytic reaction, their adsorption behaviors toward BPA were investigated. As seen in Fig. S6, the removal rates of only 3.5–4.1% demonstrated a low adsorption capacity, which eliminated the interference of adsorption on catalytic degradation. As illustrated in Fig. S7, in terms of degradation curves, they exhibited similar and almost overlapping profiles with/without pre-adsorption. Hence, the degradation experiments were implemented without pre-adsorption process. In addition, no degradation was obtained upon the addition of individual PS, suggesting the inability of PS in oxidizing BPA. While the removal rate was increased to 35.1% in CF-0 activating PS system (Fig. 3a). Promisingly, F doping promoted the degradation efficiencies greatly, corresponding to CF-0.2 (74.0%, 0.0269 min^{-1}) < CF-0.5 (84.9%, 0.0384 min^{-1}) < CF-1.5 (98.8%, 0.0798 min^{-1}) < CF-1.0 (99.5%, 0.0823 min^{-1}) (Fig. 3a-b). The synergy constant (Q) between CF-1.0 and PS was calculated to be 99.1%, revealing a strongly synergistic effect (Text S7 and Eq. S1). To establish the correlation between F doping and carbocatalytic activity, plotting the $\ln k_{\text{obs}}$ versus F content and semi-ionic C-F/covalent C-F ratio were shown in Fig. 3c-d. As depicted in Fig. 3c, a superb linearity with $R^2 = 0.9291$ and 95% confidence intervals strongly warranted the function of F doping in enhanced catalysis. To the best of our knowledge, F with large electronegativity ($\chi_F: 4.00 > \chi_C: 2.55$) can grab electrons from adjacent carbon and result in positively charged carbon, which manifests strong coupling effect with PS and functions as active sites for direct electron transfer oxidation process in N-doped carbon-based persulfate system [22]. Moreover, the defect edge induced by F doping can also act as active centers for PS activation. Presumably, such promotion in

catalytic activity should be attributed to the positively charged carbon and structure defect sites. In parallel, the fitting between $\ln k_{\text{obs}}$ and semi-ionic C-F/covalent C-F also exhibited a good linear correlation with $R^2 = 0.9138$ and more than 95% confidence level, implying a significant role of semi-ionic C-F.

3.3. Catalytic mechanisms

3.3.1. Quenching experiments

The chemical quenching experiments were implemented to discriminate the reactive species during BPA oxidation. Herein, methanol (MeOH) was utilized to detect the presence of $\text{SO}_4^{\bullet-}$ ($k = 3.2 \times 10^6 \text{ M}^{-1} \text{ s}^{-1}$) and $\bullet\text{OH}$ ($k = 9.7 \times 10^8 \text{ M}^{-1} \text{ s}^{-1}$), while *tert*-butanol (TBA) was regarded as a scavenger of $\bullet\text{OH}$ ($k = 3.8\text{--}7.6 \times 10^8 \text{ M}^{-1} \text{ s}^{-1}$) rather than $\text{SO}_4^{\bullet-}$ ($k = 8 \times 10^5 \text{ M}^{-1} \text{ s}^{-1}$) [36]. As displayed in Fig. 4a-b, in CF-0/PS/BPA system, BPA degradation was significantly inhibited after adding MeOH and TBA, and the removal rates decreased from 35.1% to 13.9% and 31.4%, respectively, implying the critical role of $\text{SO}_4^{\bullet-}$ and $\bullet\text{OH}$. By contrast, in terms of F-contained carbons CF-X, MeOH and TBA exerted a little influence on BPA removal with 0.7–9.7% reduction. This case confirmed that BPA oxidation in CF-X/PS/BPA system did not rely on the radicals. Meanwhile, the similar scenario also happened in the presence of *L*-histidine as $^1\text{O}_2$ scavenger (7.0%–13.2% decline) [37], which revealed the minor contribution of $^1\text{O}_2$. Considering the secondary roles of $\text{SO}_4^{\bullet-}$, $\bullet\text{OH}$, and $^1\text{O}_2$ in the fluorinated carbocatalytic PS activation, it definitely existed other species behind BPA degradation. To this end, the electron transfer oxidation process was studied, and it was a widely acceptable and plausible way in oxidizing the electron-rich contaminant (phenols and amines). The Cl element of NaClO_4 possesses the highest valence (VII) state, which enables it to accept the electron on the surface of catalyst, resulting in the reduction of NaClO_4 into ClO_3^- , ClO_2^- , and ClO^- . Herein, NaClO_4 was used as free-electron scavenger. BPA degradation was suppressed remarkably in CF-1.0/PS/BPA system by

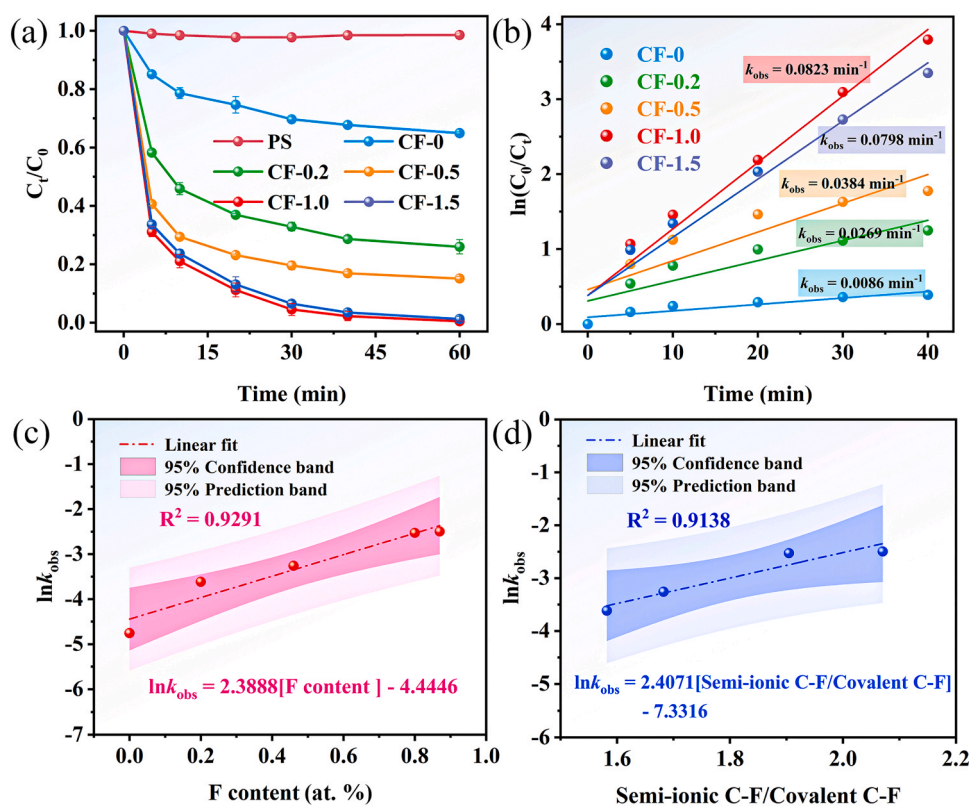


Fig. 3. (a) BPA degradation in different systems; (b) Degradation rates of BPA in various conditions; (c) Correlation of $\ln k_{\text{obs}}$ versus F content; (d) Relationship between $\ln k_{\text{obs}}$ and semi-ionic C-F/covalent C-F ratio. Reaction conditions: [BPA] = 20 mg L^{-1} , [PS] = 0.5 mM , [Catalyst] = 0.3 g L^{-1} , initial solution pH = 6.34.

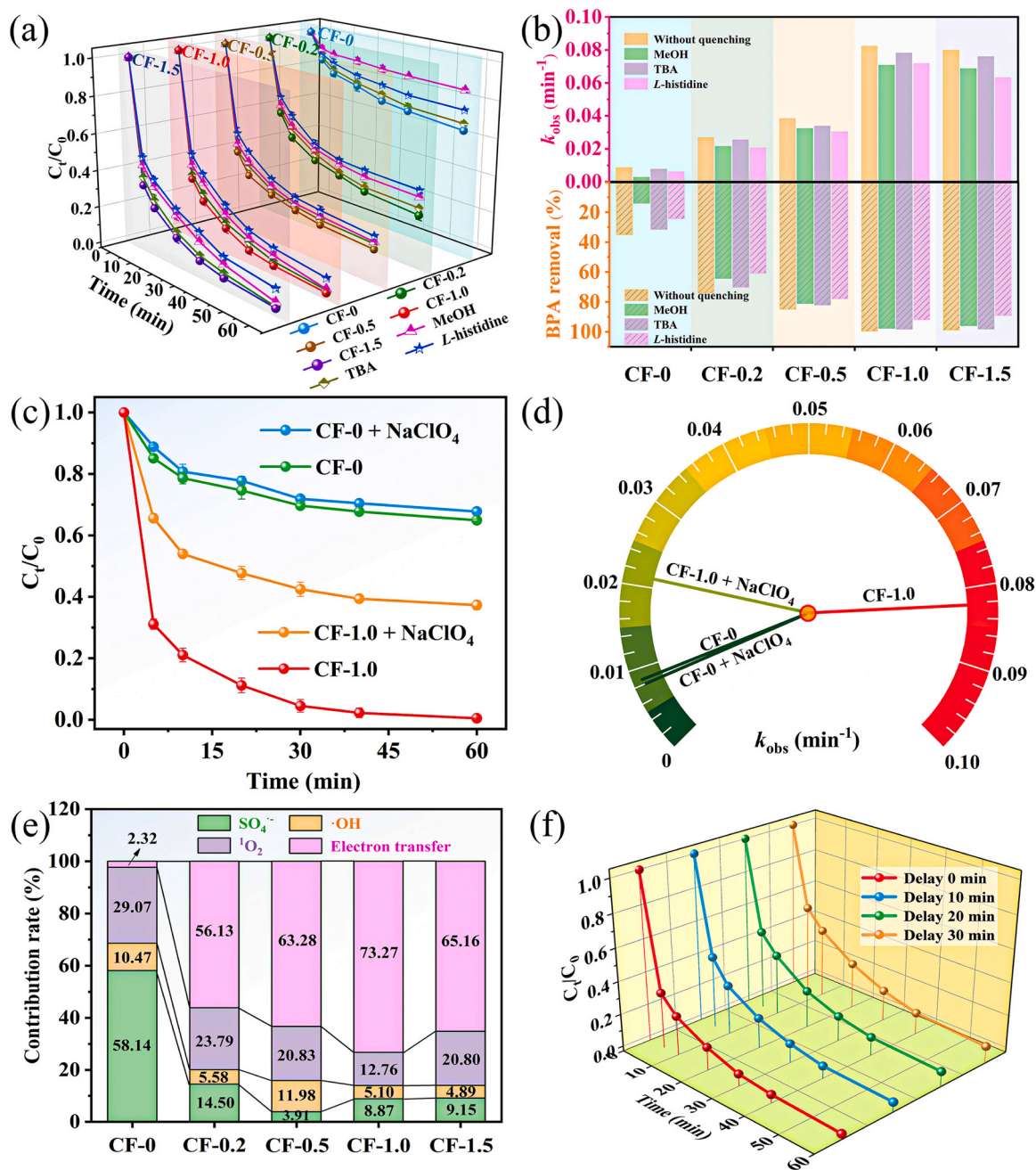


Fig. 4. Effect of scavengers on catalytic degradation of BPA (a); BPA removal percentages and the corresponding k_{obs} in different quenching systems (b); Quenching effect of NaClO₄ (c); Corresponding k_{obs} after adding NaClO₄ (d); Relative contribution percentages of various species toward BPA oxidation (e); Delaying experiments at 0, 10, 20, and 30 min (f). Reaction conditions: [BPA] = 20 mg L⁻¹, [PS] = 0.5 mM, [MeOH] = [TBA] = 0.25 M, [L-histidine] = 10 mM, [NaClO₄] = 10 mM, [Catalyst] = 0.3 g L⁻¹, initial solution pH = 6.34.

adding NaClO₄, accompanying a steep decline in removal rates from 99.5% (0.0823 min⁻¹) to 62.7% (0.0212 min⁻¹) (Fig. 4c-d). It was a powerful evidence that electron transfer dominated BPA degradation in F-doped carbon-catalyzed PS system. To further clarify the function of electron transfer, the contribution percentages of various species to BPA oxidation were calculated in line with the Eqs. S2-S5 (Text S8). Notably, the proportions of electron transfer were up to 56.13%–73.27% in F-embedded carbons (Fig. 4e). While this value was as low as 2.32% in CF-0-involved reaction system, agreeing well with the negligible inhibition with NaClO₄. Such opposite results clearly unveiled that F doping facilitates the mechanism transformation from radical to electron-transfer nonradical oxidation. In addition to SO₄^{•-}, •OH, ¹O₂, and electron transfer, superoxide anion radical (O₂^{•-}) is also an

important reactive species in carbon-driven PS activation. The scavenging experiments of *p*-benzoquinone (BQ) demonstrated the existence of O₂^{•-} ($k = 9 \times 10^8$ M⁻¹ S⁻¹), but it was deemed as a precursor for ¹O₂ formation rather than oxidizing pollutant directly (Fig. S8) [38]. Thus O₂^{•-} contribution toward BPA degradation was not in consideration.

In order to prove the occurring electron transfer process, the delaying experiments were performed (Fig. 4 f). Under these conditions, BPA was not immediately added into CF-1.0/PS mixture, but was placed in the designated time intervals (10 min, 20 min, and 30 min). In principle, if •OH, SO₄^{•-}, and ¹O₂ acted as the primary reactive species, such delays should deteriorate this oxidation to a large extent, on account of the invalid active sites consumption and the resultant ROS concentration reduction. Distinctively, the oxidative behavior based on electron-

transfer process was less susceptible to the delaying experiments, since the catalytic reaction merely initiates after adding contaminants. As expected, there appeared a slightly suppressed BPA oxidation by only 2.6–7.1% in CF-1.0/PS system, further certifying the electron-transfer nonradical process contributing to BPA degradation.

3.3.2. EPR analysis

The electron paramagnetic resonance (EPR) spectrum was conducted to further identify the reactive oxygen species (ROS) in the course of PS activation. DMPO (5,5-dimethyl-pyrroline-oxide) was used to capture the $\cdot\text{OH}$, $\text{SO}_4^{\cdot-}$, and $\text{O}_2^{\cdot-}$. As illustrated in Fig. 5a, no signal peaks appeared in solo DMPO and DMPO+PS systems. As the addition of CF-0, two characteristic peaks of DMPO-OH ($\alpha_{\text{H}} = \alpha_{\text{N}} = 14.9$ G) and DMPO-SO₄ ($\alpha_{\text{H}} = 9.6$ G, $\alpha_{\text{H}} = 1.48$ G, $\alpha_{\text{N}} = 0.78$ G, $\alpha_{\text{N}} = 13.2$ G) were noted, showing the formation of $\cdot\text{OH}$ and $\text{SO}_4^{\cdot-}$ [39]. Surprisingly, the peaks of DMPO-SO₄ and DMPO-OH were absent in CF-1.0/PS/DMPO system. Instead, a seven-line signal peak with an intensity ratio of 1:2:1:2:1:2:1 was observed, which could be ascribed to the oxidation peak of DMPO, namely DMPO-X. As previously reported, $^1\text{O}_2$ could oxidize DMPO into DMPO-X [40]. At the same time, the direct electron transfer mediated by carbon-activated PS complex was also responsible for DMPO oxidation [21]. To figure out the origin of DMPO-X, the produced $^1\text{O}_2$ was firstly determined by TEMP (4-hydroxy-2,2,6,6-tetramethylpiperidine)

trapping agent. An equal intensity three-line signal peak (1:1:1) emerged in both CF-0 and CF-1.0, belonging to the adduct of TEMP- $^1\text{O}_2$ ($\alpha_{\text{N}} = \alpha_{\text{N}} = \alpha_{\text{N}} = 16.9$ G) (Fig. 5b). Furthermore, the signal intensity in CF-1.0/PS system was much higher than that in CF-0/PS system, indicating the more $^1\text{O}_2$ generation and better catalytic activity of CF-1.0. Another reactive species $\text{O}_2^{\cdot-}$ was monitored in pure MeOH to exclude the inference of $\cdot\text{OH}$ and $\text{SO}_4^{\cdot-}$. As depicted in Fig. 5c, the characteristic peak of DMPO- $\text{O}_2^{\cdot-}$ ($\alpha_{\text{N}} = 14.3$ G, $\alpha_{\text{H}} = 11.2$ G, $\alpha_{\text{H}} = 1.3$ G) confirmed the presence of $\text{O}_2^{\cdot-}$. As a whole, the EPR results verified the involvement of $\cdot\text{OH}$, $\text{SO}_4^{\cdot-}$, $\text{O}_2^{\cdot-}$, and $^1\text{O}_2$ during the activation process. Nonetheless, none of them acted as the main active substances for BPA degradation in CF-1.0/PS/BPA system in combination with the outcomes of quenching test.

3.3.3. Electron transfer process

In light of the above results, it was ascertained that the electron transfer process played a dominant role on BPA removal by F-doped carbon activating PS. Latest research demonstrated that electron transfer mechanism is derived from the formed carbon surface-activated PS complex ($\text{C-S}_2\text{O}_8^{2-*}$) with a high redox potential, and it abstracts electron from pollutant to initiate the oxidation [41]. To address this issue, *in-situ* Raman spectrum of carbocatalyst was recorded to confirm the meta-stable $\text{C-S}_2\text{O}_8^{2-*}$. As seen in Fig. 5d-e, the characteristic peaks of PS were

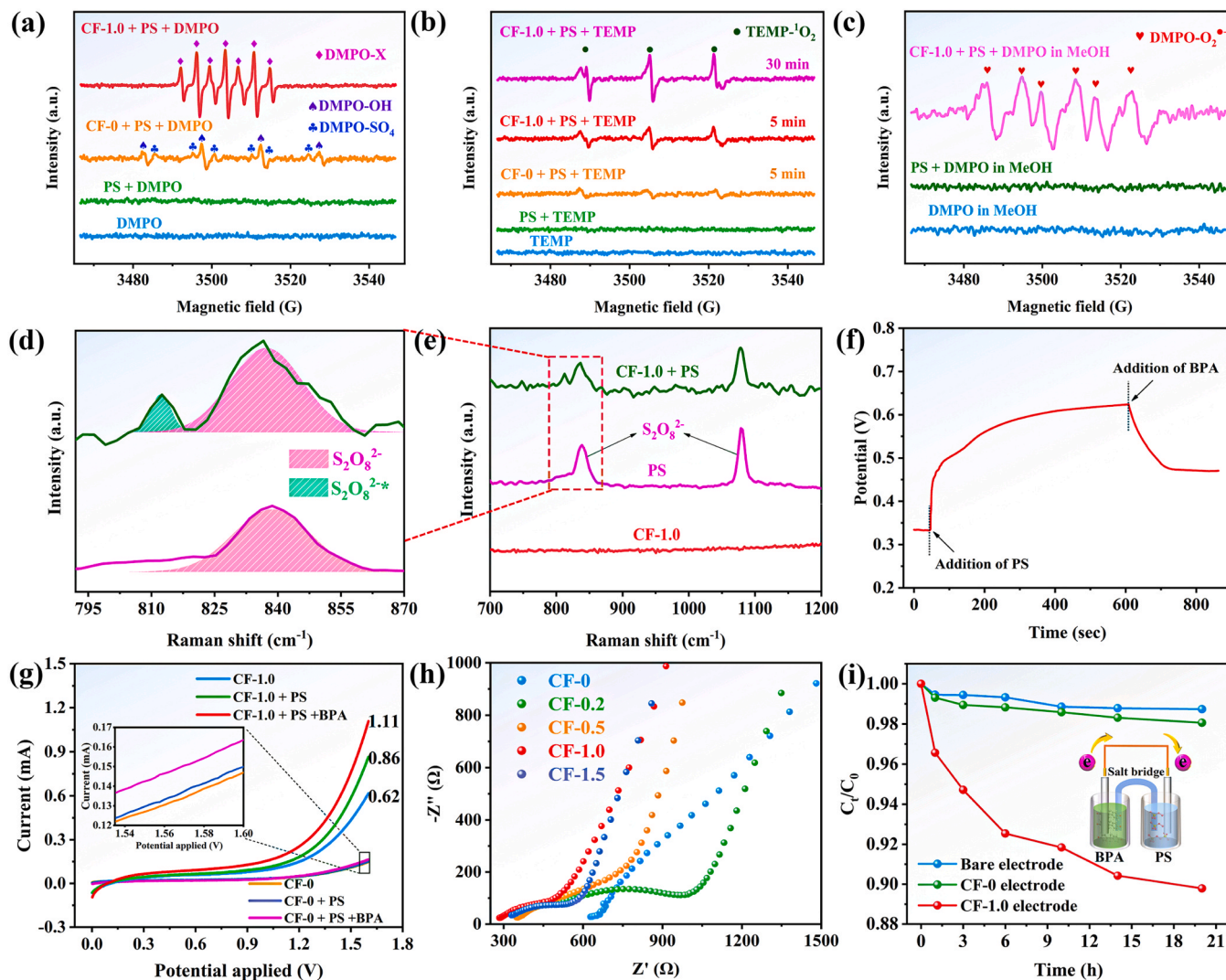


Fig. 5. Spin-trapping EPR spectra for $\text{SO}_4^{\cdot-}/\cdot\text{OH}$ (a), $^1\text{O}_2$ (b), and $\text{O}_2^{\cdot-}$ (c); In-situ Raman spectra (d-e); Open circuit potential by adding PS and BPA (f); Linear sweep voltammetry (g); EIS Nyquist plots (h); BPA degradation in the galvanic oxidation reactors (i). Reaction conditions: [BPA] = 20 mg L⁻¹, [PS] = 0.5 mM, [Catalyst] = 0.3 g L⁻¹, [DMPO] = [TEMP] = 50 mM, initial solution pH = 6.34.

located at 837 cm^{-1} and 1078 cm^{-1} , while one more peak emerged near 813 cm^{-1} when coupled with CF-1.0. The new blue-shift peak was originated from the vibration of the extended peroxide O-O bond in PS ($\text{O}_3\text{S-O-O-SO}_3$), which corroborated the formation of $\text{CF-1.0-S}_2\text{O}_8^{2-}$ [42]. In addition, the generated $\text{C-S}_2\text{O}_8^{2-}$ complex was also confirmed by electrochemical analysis. From the *in-situ* open circuit potential (OCP) curve of CF-1.0, the injection of PS into CF-1.0 solution enhanced the potential sharply from 0.33 V to 0.62 V, which resulted from the formation of $\text{CF-1.0-S}_2\text{O}_8^{2-}$ with a higher oxidative power, implying the strong interaction between CF-1.0 and PS (Fig. 5f). As similarly discovered by He et al., it was reasonable that further adding BPA triggered a decrease of potential to 0.47 V [4]. In this situation, the adsorbed-PS on carbon surface was reduced into SO_4^{2-} originating from the dual-electron-transfer from BPA to PS, leading to the decomposition of $\text{CF-1.0-S}_2\text{O}_8^{2-}$ and the decline in open potential.

Besides OCP measurement, the electron transfer process in CF-1.0/PS/BPA system was also elucidated through linear scanning voltammetry (LSV). As displayed in Fig. 5g, inconspicuous current responses were noted in both CF-0, CF-0/PS, and CF-0/PS/BPA systems at the operating voltage of 0–1.6 V, implying the absence of electron transfer. In contrast, the current had an evident increase from 0.62 mA to 0.86 mA with simultaneous presence of CF-1.0 and PS (CF-1.0/PS). That was the result of electron transfer between catalyst and persulfate, as evidenced by the electron transfer number in DFT analysis. Moreover, this value was further increased to 1.11 mA accompanying BPA addition, which revealed the electron transfer effect occurring in CF-1.0/PS/BPA system. In essence, carbon material serves as the electron shuttle to mediate the electron transfer from pollutant to persulfate, thus the conductivity is an essential factor affecting electron transfer effectiveness. Their electrochemical impedance spectroscopy (EIS) were shown

in Fig. 5h. In EIS Nyquist curve, the smaller radius of semicircle means the higher conductivity. Obviously, F doping positively promoted the electroconductibility of catalysts, whose orders were $\text{CF-1.0} > \text{CF-1.5} > \text{CF-0.5} > \text{CF-0.2} > \text{CF-0}$, favoring the resultant electron transfer.

Aiming at verifying the speculative mechanism once more, BPA degradation was performed in a galvanic oxidation reactor, in which PS and BPA solutions were divided into two half-cells rather than mixing evenly, so BPA could only be oxidized via the electron transfer pathway (Fig. 5i). On the condition of blank electrode and CF-0-wrapped electrode, no BPA degradation was present. However, using CF-1.0-modified glass carbon as the working electrode, the removal rate of BPA was increased to 10.2%. This suggested that BPA was oxidized via electron transfer only in CF-1.0-engaged system. To sum up, benefiting from CF-1.0- $\text{S}_2\text{O}_8^{2-}$ and the enhanced conductivity of carbocatalyst, F doping gave an impetus to induce a mechanism transformation from radical to electron transfer. Such conversion was also correlated with the positively charged carbon neighboring F and discussed in DFT calculation.

3.3.4. Active sites determination

The stability of CF-1.0 was evaluated by cyclic durability experiments (Fig. S9). The removal rate of BPA reduced to 83.7% and 73.7% in the 2nd and 3rd runs, respectively. As shown in Fig. S10, the PS decomposition rates in the used CF-1.0 activating PS systems were only 63.2%–73.1%, agreeing well with the low removal efficiency. In addition, the zeta potential (pH_{zpc}) of 3rd CF-1.0 was 4.06, thus excluding the electrostatic repulsion-caused degradation inhibition (Fig. S11). As seen the ^{19}F NMR spectrum, the signal peaks of F were absent in the two systems (PS/BPA and filtered CF-1.0/PS/BPA using $0.22\text{ }\mu\text{m}$ filter membrane) (Text S9 and Fig. S12). This case indicated that nucleophilic substitution of F was not the reason accounting for

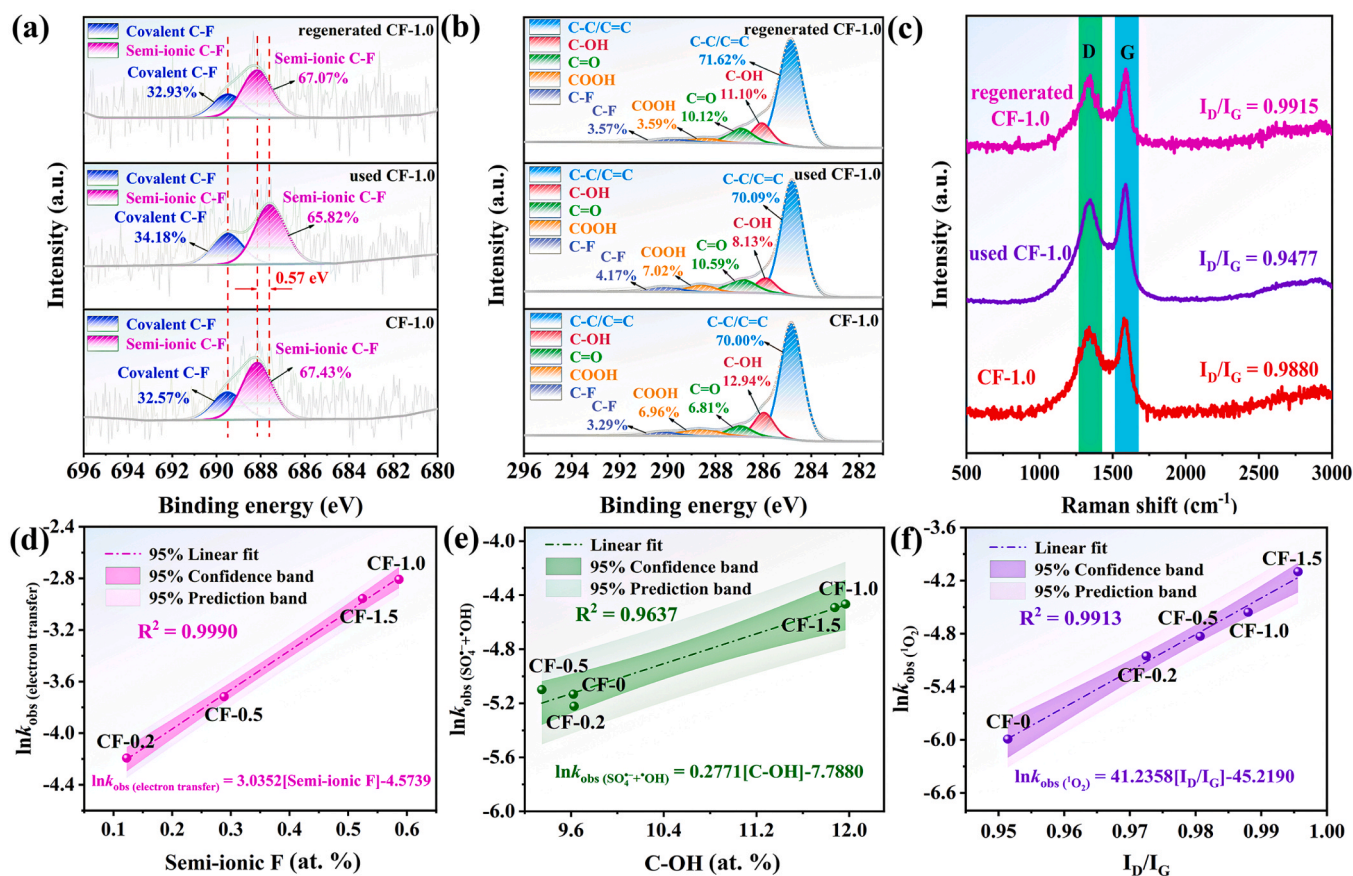


Fig. 6. F 1s XPS (a), C 1s XPS (b), and Raman spectrum (c) for raw, used, and regenerated CF-1.0; Correlation of $\ln k_{\text{obs}}$ (electron transfer) versus semi-ionic F percentage (d), $\ln k_{\text{obs}} (\text{SO}_4^{\cdot-} \cdot \text{OH})$ versus C-OH content (e), and $\ln k_{\text{obs}} (^1\text{O}_2)$ versus I_D/I_G value (f).

catalyst deactivation.

To further elucidate such deactivation, the variations of functional groups, structural defects, and S_{BET} of carbocatalyst before and after use were investigated. Fig. 6a depicted the F 1 s high resolution XPS spectrum, and the bonding energy of covalent C-F remained almost invariable after reaction. However, the semi-ionic C-F feature of the used CF-1.0 shifted toward lower binding energy about 0.57 eV, signifying the increase of electron cloud density on semi-ionic C-F after reaction. As a plausible explanation, F-doped carbon could enable BPA transfer electrons to CF-1.0- $\text{S}_2\text{O}_8^{2-}$ during catalytic degradation, resulting in an elevated electron density for semi-ionic C-F. Pioneering document mentioned the more superior catalytic activity of semi-ionic C-F relative to covalent C-F [31]. Thus, semi-ionic C-F was supposed to be the reactive site in activating PS. In addition, the oxygen content of used CF-1.0 was approximately 2-folds higher than that of fresh CF-1.0 (6.64–13.50%) (Table S2). Excessive oxygen was not in favor of catalysis. On the one hand, the conductivity of carbonaceous material will be deteriorated [21]. On the other hand, the superfluous oxygen groups will occupy the reaction edges and prohibit the interaction with PS by spatial hindrance effect [43]. After reaction, the proportion of C-OH declined from 12.94% to 8.13%, in contrast to the increase of C=O from 6.81% to 10.59% (Fig. 6b). As known, C-OH group can be oxidized into C=O and simultaneously donate one electron to reduce persulfate into $\text{SO}_4^{\cdot-}$ radical [21,44]. Herein, the evolution of C-OH to C=O revealed that C-OH might work as catalytic site for radical generation. As seen in Raman spectra (Fig. 6c), the $I_{\text{D}}/I_{\text{G}}$ value decreased from 0.9880 to 0.9477 after reaction, proving a significant role of structural defect in PS activation. It was reported that the structural defect (zigzag edges and armchair edges) possesses delocalized π -electron, which can accept electrons of persulfate and induces the generation of $^1\text{O}_2$ as a result [29,45]. In a word, the semi-ionic C-F, C-OH, and structural defects were determined to be the active centers participating in PS activation. In addition, the coverage of active sites on catalyst surface was an additional aspect with respect to this catalyst deactivation, described by S_{BET} orders: $207.13 \text{ m}^2 \text{ g}^{-1}$ for used CF-1.0 < $501.58 \text{ m}^2 \text{ g}^{-1}$ for raw CF-1.0 (Table S1).

Noticeably, one-step thermal treatment (700°C for 2 h under N_2 atmosphere) improved the BPA removal efficiency to 95.0% by regenerated-CF-1.0 activating PS. In the meanwhile, the active functional groups of catalyst were re-constructed, such as the correction of semi-ionic C-F binding energy about 0.57 eV red-shift, the enhancement of C-OH content from 8.13% (3rd CF-1.0) to 11.10% (regenerated CF-1.0), and the structure defect increment from 0.9477 to 0.9915 ($I_{\text{D}}/I_{\text{G}}$) (Fig. 6a-c). The reversible conversion of active groups contributed to the enhanced catalytic performance. As such, that confirmed both semi-ionic C-F, C-OH, and structural defects acted as active centers for PS activation once again. As shown in Fig. S13a, the proportion of C-OH decreased from 10.54% to 5.22% after reaction, while it was increased to 11.62% through heat treatment. In parallel, the C=O content exhibited an opposite trend, rising from 9.43% to 24.97% (used catalyst) and then declining from 24.97% to 7.92% (regenerated catalyst). Moreover, the $I_{\text{D}}/I_{\text{G}}$ value exhibited similar variations, as demonstrated by a reduction from 0.9514 to 0.9326 after reaction and a recovery to 0.9609 after regeneration (Fig. S13b). As a result, as for CF-0, C-OH and structural defects were determined to be the reactive sites participating in PS activation.

To reveal the respective reactive sites behind radical and nonradical pathways, $\ln k_{\text{obs}}$ was utilized as a descriptor to establish the quantitative structure-activity relationships (QSARs). Wherein, the k_{obs} (electron transfer), k_{obs} ($\text{SO}_4^{\cdot-}$ OH), and k_{obs}^1 (O_2) were the product of k_{obs} (without quencher) and contribution rate for each species (Seen Fig. 4e). Fig. 6d-f showed that semi-ionic C-F percentage, C-OH proportion, and $I_{\text{D}}/I_{\text{G}}$ value had excellent linearity with $\ln k_{\text{obs}}$ (electron transfer), $\ln k_{\text{obs}}$ ($\text{SO}_4^{\cdot-}$ OH), and $\ln k_{\text{obs}}^1$ (O_2), respectively, whose R^2 corresponded to 0.9990, 0.9637, and 0.9913. Such high R^2 revealed that semi-ionic C-F favors the electron transfer, C-OH facilitates the transformation of PS into $\text{SO}_4^{\cdot-}/^{\cdot}\text{OH}$,

and structural defects induce the non-radical $^1\text{O}_2$ production. As a complement, the correlations of $\ln k_{\text{obs}}$ and other two parameters were also plotted. As predicted, when fitting $\ln k_{\text{obs}}$ (electron transfer) with C-OH proportion and $I_{\text{D}}/I_{\text{G}}$ value, the R^2 decreased from 0.9990 to 0.7836 and 0.8365 (Fig. S14a-b). Likewise, a relative inferior R^2 could be observed by plotting $\ln k_{\text{obs}}^1$ ($\text{SO}_4^{\cdot-}$ versus semi-ionic C-F and $I_{\text{D}}/I_{\text{G}}$ (0.9302 and 0.5669) (Fig. S14c-d), as well as $\ln k_{\text{obs}}$ (versus semi-ionic C-F and C-OH (0.6721 and 0.5006) (Fig. S14e-f). To be specific, the results of QSARs analysis powerfully claimed that semi-ionic C-F, C-OH, and structural defects function as electron transfer channel, $\text{SO}_4^{\cdot-}/^{\cdot}\text{OH}$, and $^1\text{O}_2$ formation site, respectively. Moreover, it is ascertained that the improvement of catalytic activity was mainly governed by improving electron transfer ability along with F doping (Text S10 and Fig. S15).

3.3.5. Theoretical calculations

Density functional theory (DFT) calculation was adopted to reveal how to reinforce the electron-transfer regime by F-doping. To improve the accuracy of the calculation, the effect of solvation was considered in the DFT calculation. Fig. 7 depicted the PS adsorption model on pristine carbon (CF-0) and F-doped carbon (CF-X). Obviously, the adsorption energy (E_{ads}) of PS on F-doped carbon (-5.380 eV) is higher than that on pristine carbon (-5.220 eV). The result implied that PS is more readily adsorbed on F-doped carbon, promoting the formation of carbon-activated persulfate complex (C-PS*). Also, compared to the O-O bond length (1.470 \AA) of PS adsorbed on pristine carbon, this value on F-doped carbon became more longer (1.480 \AA), suggesting that PS more readily decomposes on the fluorinated carbon. Owing to the large electronegativity of F, the incorporation of F atom can result in the electron-deficient carbon in adjacent. With F doping, the Bader charge of the corresponding carbon atom C_1 and C_2 had a decrease from 3.861 eV to 3.712 eV and 4.131 to 3.559 eV (Table 1). After PS was attached to the surface of F-doped carbon, the Bader charge of F atom declined by 0.092 eV (F_1 from 7.669 eV to 7.620 eV and F_2 from 7.657 eV to 7.614 eV), and this value in adjacent carbon decreases by 0.004 eV . Therefore, once formed C-PS*, the existing electron loss of 0.096 eV will offer a driving force to boost contaminant spontaneously transfer electron to carbonaceous matrix (BPA \rightarrow C). Of which, the electron-deficient semi-ionic C-F acted as the electron transfer shuttle. However, before and after the coupling of CF-0 to PS, the Bader charge of the designated carbon atom increases by 0.150 eV (C_1 : $3.861 \text{ eV} \rightarrow 4.107 \text{ eV}$ and C_2 : $4.131 \text{ eV} \rightarrow 4.035 \text{ eV}$). The positive increase of charge demonstrated that pristine carbon was lack of the impetus for electron transfer, in agreement with the radical-dominated pathways in CF-0/PS/BPA system. In addition, the electron transfer number from F-doped carbon to PS was 1.980 e , which was higher than that of the pristine carbon (0.020 e). Such result indicated that F-doping improves the ability of carbocatalyst in transferring electron to PS (C \rightarrow PS). Consequently, benefiting from the enhanced two-step electron-transfer from BPA to CF-1.0 and CF-1.0 to PS (BPA \rightarrow C \rightarrow PS), there realized the nonradical oxidation degradation of BPA via electron-transfer regime.

3.3.6. Activation mechanism

Based on the above analysis, the possible reaction mechanism in CF-1.0/PS system was proposed and depicted in Scheme 2. F doping switched the activation mechanism from radical persulfate-activated process into electron transfer-dominated nonradical process. Firstly, thanks to the electrostatic interaction, PS was adsorbed on the carbocatalyst surface to form the carbon-activated persulfate complex (C- $\text{S}_2\text{O}_8^{2-}$). Stimulated by the incorporation of F atom creating the electron-deficient carbon layer, the electron-rich BPA tended to transfer electron to C- $\text{S}_2\text{O}_8^{2-}$, in an effort to balance the electron loss in the carbonaceous matrix, thereby realizing the oxidative degradation of pollutant and PS decomposition (Eq. 1). Wherein, the semi-ionic C-F served as an electron shuttle channel to mediate dual electron transfer from BPA to PS. Secondly, the structure defect-driven PS activation was the other nonradical pathway in BPA oxidation. In the case, the suspended σ -bond of

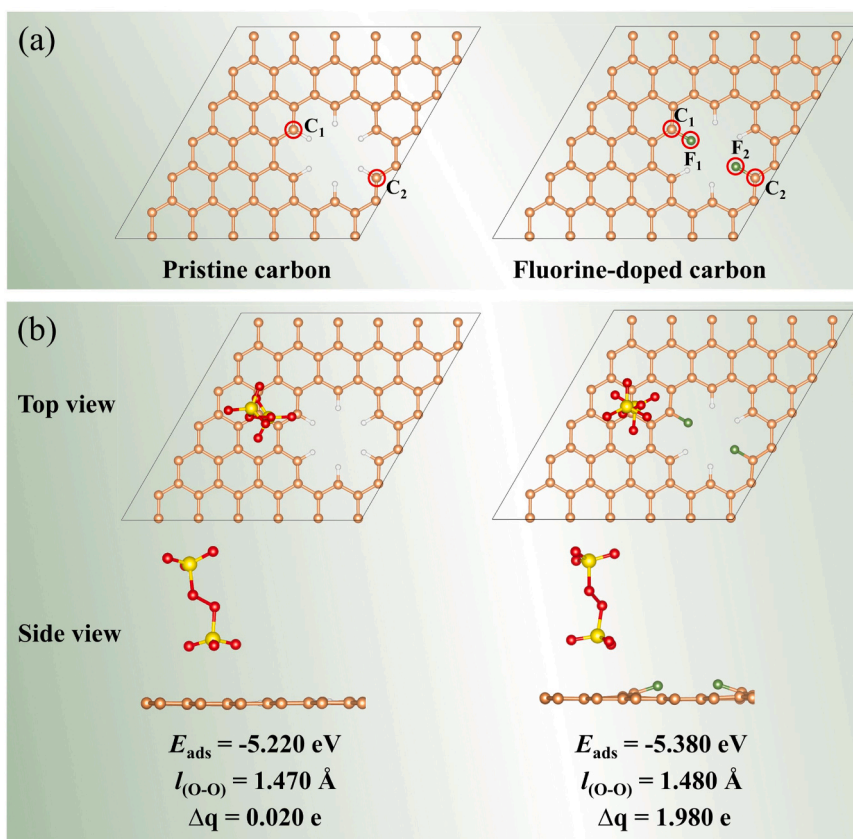


Fig. 7. (a) Optimized molecular model of pristine carbon (CF-0, left) and F-doped carbon (CF-X, right); (b) PS adsorption on CF-0 and CF-X. Inset: top view (up), side view (down), E_{ads} stands for the adsorption energy (eV), $l_{\text{(O-O)}}$ refers to the bond length of peroxy bond (O-O) in persulfate, and Δq corresponds to the electron transfer number.

Table 1

Bader charges of F and C atom before and after coupled with PS.

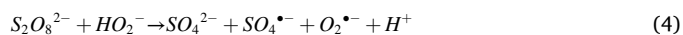
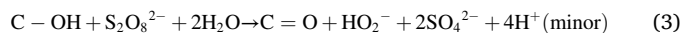
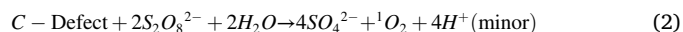
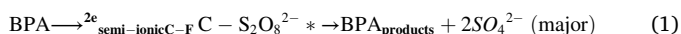
Models	Bader charge (e)			
	F ₁	F ₂	C ₁	C ₂
Pristine carbon/PS	-	-	3.861 ^a / 4.107 ^b	4.131 ^a / 4.035 ^b
F-doped carbon/PS ^c	7.669 ^a / 7.620 ^b	7.657 ^a / 7.614 ^b	3.712 ^a / 3.633 ^b	3.559 ^a / 3.634 ^b

^a Bader charge before coupled with PS.

^b Bader charge after coupled with PS.

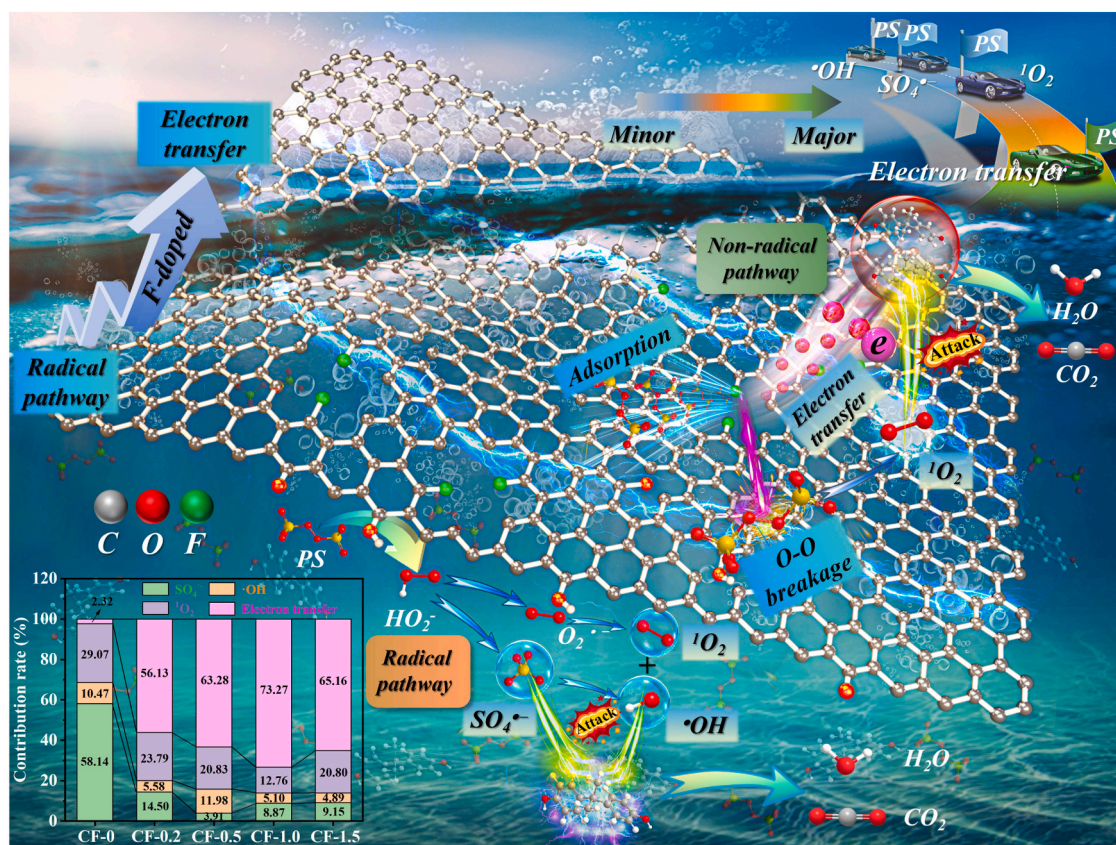
^c C is adjacent to F.

structural defect created a π -electron delocalized region, which could accept the electrons from PS, rendering PS oxidation and $^1\text{O}_2$ production (Eq. 2) [29]. For radical pathway, the C-OH and H_2O acted as the electron donor to reduce PS, resulting in the generation of hydroperoxide anion (HO_2^-), sulfate (SO_4^{2-}), and carbonyl group ($\text{C}=\text{O}$) (Eq. 3) [21]. Subsequently, the resultant HO_2^- further reacted with $\text{S}_2\text{O}_8^{2-}$ to get $\text{SO}_4^{\bullet-}$ and $\text{O}_2^{\bullet-}$ (Eq. 4), in which $\text{O}_2^{\bullet-}$ was commonly viewed as the precursor of $^1\text{O}_2$ production via self-recombination with H_2O rather than oxidizing organics itself (Eq. 5) [12]. In addition, the $\bullet\text{OH}$ was derived from the reaction of $\text{SO}_4^{\bullet-}$ with H_2O (Eq. 6) [12]. On the basis of the chemical quenching, EPR, and electrochemical analysis, one could conclude that the electron transfer pathway dominated the BPA oxidation, whereas $^1\text{O}_2$, $\text{SO}_4^{\bullet-}$, and $\bullet\text{OH}$ played the secondary role, reflected by the contribution rate orders: $\bullet\text{OH}$ (5.10%) < $\text{SO}_4^{\bullet-}$ (8.87%) < $^1\text{O}_2$ (12.76%) < electron transfer (73.27%) (Fig. 4e).



3.4. Influences of various factors on BPA degradation

As illustrated in Fig. 8a and Fig. S16a, BPA degradation was positively relevant to PS concentration from 0.1 mM to 0.5 mM. Nevertheless, as continually increased PS dosage to 0.7 mM and 0.9 mM, the removal efficiency was almost invariable. In this case, the number of active sites on catalyst surface restricted the further enhancement in degradation performance. Also, the CF-1.0 dosage was proportional to the removal efficiencies (Fig. 8b and Fig. S16b). The excessive active centers guaranteed the enough ROS to oxidize BPA, resulting in effective catalysis. Distinctive with PS and CF-1.0 dosage, BPA concentration exerted an opposite role in catalytic performance. As the varying concentration of 20 mg L⁻¹ to 100 mg L⁻¹, the k_{obs} gradually declined from 0.0823 min⁻¹ to 0.0089 min⁻¹ (Fig. 8c and Fig. S16c). Such visualized deterioration was the combined result of insufficient CF-1.0 and PS dosage, leading to the limited ROS production. Fig. 8d displayed the correlation between $\ln k_{\text{obs}}$ and above-mentioned three parameters. Interestingly, both $\ln[\text{PS}]$, $\ln[\text{CF-1.0}]$, and $\ln[\text{BPA}]$ manifested a well-fitted relationship with $\ln k_{\text{obs}}$ ($R^2 = 0.9240, 0.9436, \text{ and } 0.9473$), whose slope was 0.3385, 2.3878, and 1.3698, respectively. In CF-1.0/



Scheme 2. Proposed mechanism of PS activation and BPA degradation on CF-1.0.

PS/BPA system, the higher values of slopes mean that the active sites act as the predominant role affecting the reaction rate. Therefore, PS adsorption and activation on CF-1.0 was the dominant rate-limiting step.

The effect of pH on degradation performance was investigated under different pH values of 3.04, 5.00, 7.31, 9.05, and 10.94 (Fig. 8e and Fig. S16d). The degradation curve profile maintained constant from strongly acidic (3.04) to weak basic (9.05) condition, indicating a decent adaptability. However, strong basic surrounding of pH 10.94 brought a detrimental degradation, corresponding a k_{obs} reduction from 0.0825 min^{-1} (at pH 7.31) to 0.0335 min^{-1} . Such suppression was probably consistent with the zeta potential of CF-1.0 and BPA existing form at various pH. The zeta potential of CF-1.0 was measured to be 3.01, implying that the catalyst was negatively charged at solution pH > 3.01 and positively charged otherwise (Fig. S17). As for BPA, its $\text{pK}_{\text{a}1}$ and $\text{pK}_{\text{a}2}$ values were 9.6 and 10.2, thus existed mainly in the form of cations, amphiphiles, and anions at pH < 9.6 , pH 9.6–10.2, and pH > 10.2 , respectively [4]. In the case of pH 10.94, the electrostatic repulsion between BPA anion and negatively charged CF-1.0 would impede the proximity of the contaminant, keep it inaccessible the CF-1.0- $\text{S}_2\text{O}_8^{2-}$ complex, and then weaken the electron transfer effect. In this way, it was bound to lower the PS utilization. As depicted in Fig. 8f, Fig. S18, and Table S5, the decomposition rate of PS was as high as 87.1% at pH 3.04–7.31, but at a moderate level of 77.1% with pH 10.94, agreeing well with this inhibitory effect under strongly alkaline conditions. In addition, at pH 3.04–9.05, all systems were acidified with ultimate pH near 3.00. To our knowledge, PS activation by structure defect and C-OH generates hydrogen ions (H^+) (Eqs. 2–3), thereby reducing the solution pH. By contrast, this final pH value was only 6.53 at initial pH 10.94. This was caused by the inhibiting interaction induced by electrostatic repulsion between CF-1.0 and BPA, leading to inefficient catalysis and less amount of H^+ production.

Furman et al. mentioned that PS could be activated under basic condition [46]. To eliminate the interference of base on PS activation, the PS alone was added to degrade BPA at the initial solution pH of 9.11 and 10.98. As shown in Fig. S19, the degradation efficiency almost remained invariant, indicating that the base-mediated PS activation could be neglected in the CF-1.0/PS/BPA system. Also, the activation energy (E_a) was determined to be $14.54 \text{ kJ mol}^{-1}$ in the oxidative system (Text S11, Fig. S20 and Eqs. S6–S7). This indicated that the catalytic activity of CF-1.0 was insensitive to the temperature.

3.5. Influences of anions, humic acid, water matrices, and other pollutants

In actual aquatic surroundings, some anions (Cl^- , SO_4^{2-} , NO_3^- , and H_2PO_4^-) and humic acid (HA) may affect the catalytic process through active sites and ROS competition. In regard to anions- and HA-involved systems, their initial solution pH values of 4.67–8.33 were less than 10.94 that caused degradation inhibition, eliminating the pH-induced indirect disturbance on degradation performance (Table S6). Notwithstanding, the addition of Cl^- , SO_4^{2-} , NO_3^- , and H_2PO_4^- still disapprove BPA removal slightly, corresponding k_{obs} reduction from 0.0823 min^{-1} to 0.0760 – 0.0779 min^{-1} (Fig. 9a). It was attributable to the deactivation of $\text{SO}_4^{\bullet-}$ and $\bullet\text{OH}$ by radical chain transfer reaction with these anions, subsequently producing the lower oxidative potential species (Cl^\bullet , NO_3^\bullet , $\text{H}_2\text{PO}_4^\bullet$, etc.) and attenuating the catalysis (Text S12 and Eqs. S8–S14). Adversely, HA inhibited the BPA removal efficiency by 47.1%. Because HA (carboxyl and hydroxyl groups) can compete for the catalytic sites with BPA, resulting in the loss of active sites [15].

In the reported PS-AOPs, the CO_3^{2-} usually played a dual role either promoting or inhibiting pollutant degradation. Currently, the presence of CO_3^{2-} inhibited the removal efficiencies to 77.3% and 0.0309 min^{-1} (Fig. 9b). This might be concerned with $\text{O}_2^{\bullet-}$ spend by CO_3^{2-} (Eqs. S15–

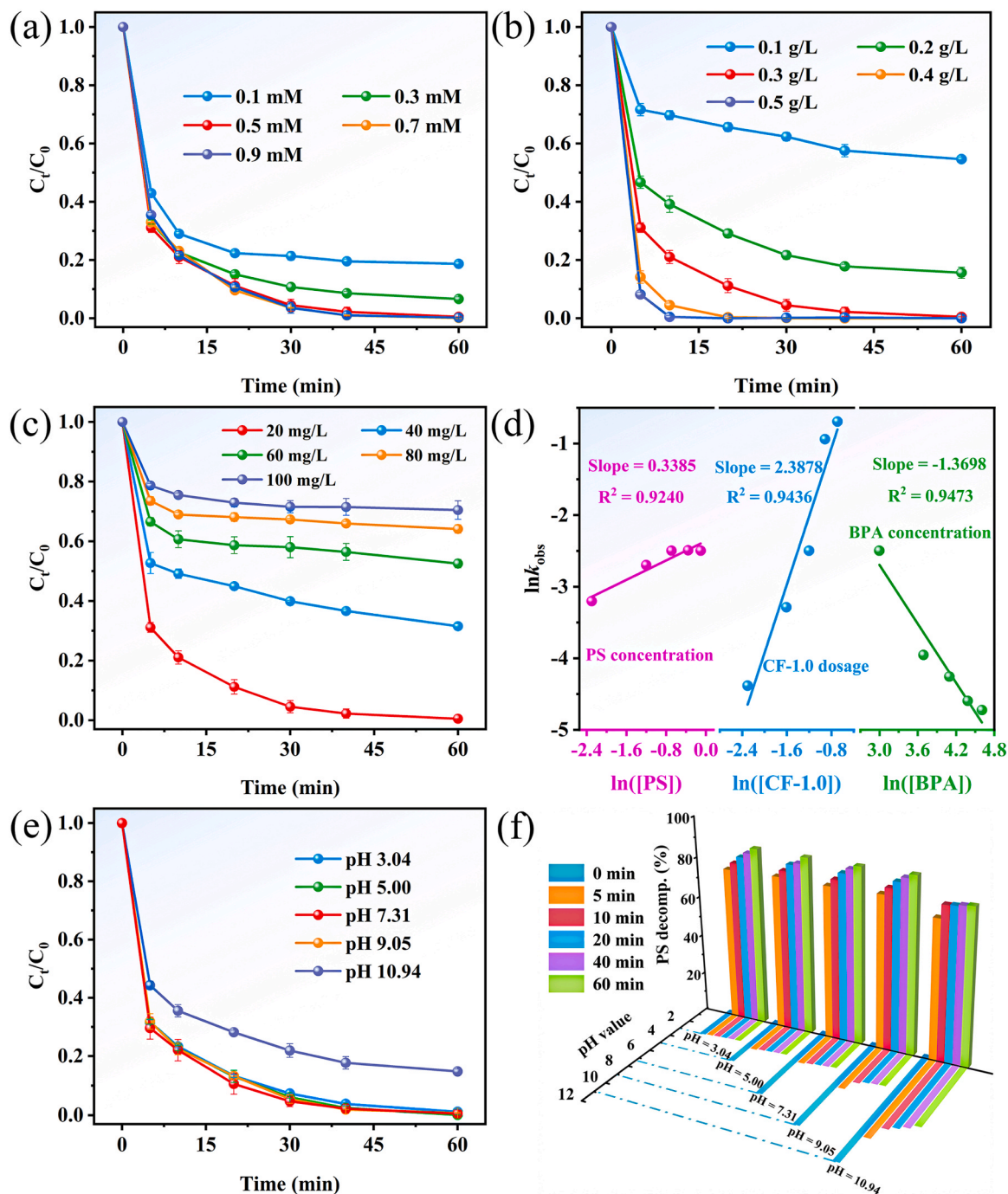


Fig. 8. Effect of PS dosage (a), catalyst dosage (b), and contaminant concentration (c) towards BPA degradation; Correlation of $\ln k_{\text{obs}}$ versus $\ln[\text{PS}]$, $\ln[\text{CF-1.0}]$, and $\ln[\text{BPA}]$ (d); Various pH influence (e); PS utilization rate and pH variations after reaction (f). Reaction conditions: $[\text{BPA}] = 20 \text{ mg L}^{-1}$, $[\text{PS}] = 0.5 \text{ mM}$, $[\text{CF-1.0}] = 0.3 \text{ g L}^{-1}$, initial solution pH = 6.34, unless particularly emphasized in the figure.

S16] [47], in which $\text{O}_2^{\bullet-}$ can recombine to generate $^1\text{O}_2$ (Eq. 5). But considering a tiny contribution rate of $^1\text{O}_2$ on BPA degradation, the consumption of partial $^1\text{O}_2$ should bring about a slight inhibition. It was contradictory with the 2.7-folds smaller k_{obs} as compared to that without CO_3^{2-} (0.0823 min^{-1}). Such discrepancy reflected that the $\text{O}_2^{\bullet-}$ quenching by CO_3^{2-} was not the principal factor. Secondly, the initial solution pH of 10.79 was closer to inhibitory value of 10.94, thus the CO_3^{2-} -created strong basic condition possibly rendered the reverse side for BPA removal. To elucidate it, the solution was adjusted to pH 8.68 that not cause any inhibition, and the removal efficiency was increased to 94.7% (0.0626 min^{-1}). Interestingly, this cure profile was almost overlapped with HCO_3^- -involved system. On the basis of carbonate

equilibrium ($\text{CO}_2\text{-HCO}_3\text{-CO}_3^{2-}$) in aqueous solution (Fig. 9c), CO_3^{2-} was converted into HCO_3^- on condition of pH 8.68, resulting in the similar degradation behaviors in the presence of HCO_3^- and CO_3^{2-} (pH 8.68). In spite of many efforts, it was still frustrating to figure out the pH effect in CO_3^{2-} system due to carbonate equilibrium interference. Fig. 9d depicted the EPR spectrum with and without HCO_3^- system. Upon addition of HCO_3^- , the TEMP- $^1\text{O}_2$ signal peak became weak, which implied that the quenching reaction of $\text{O}_2^{\bullet-}$ with HCO_3^- was responsible for HCO_3^- -induced inhibition.

The practicability of CF-1.0/PS system was also appraised using tap water (obtained from Dongguan University of Technology), lake water (from Dongguan Pine Lake misty rain), and diluted landfill leachate

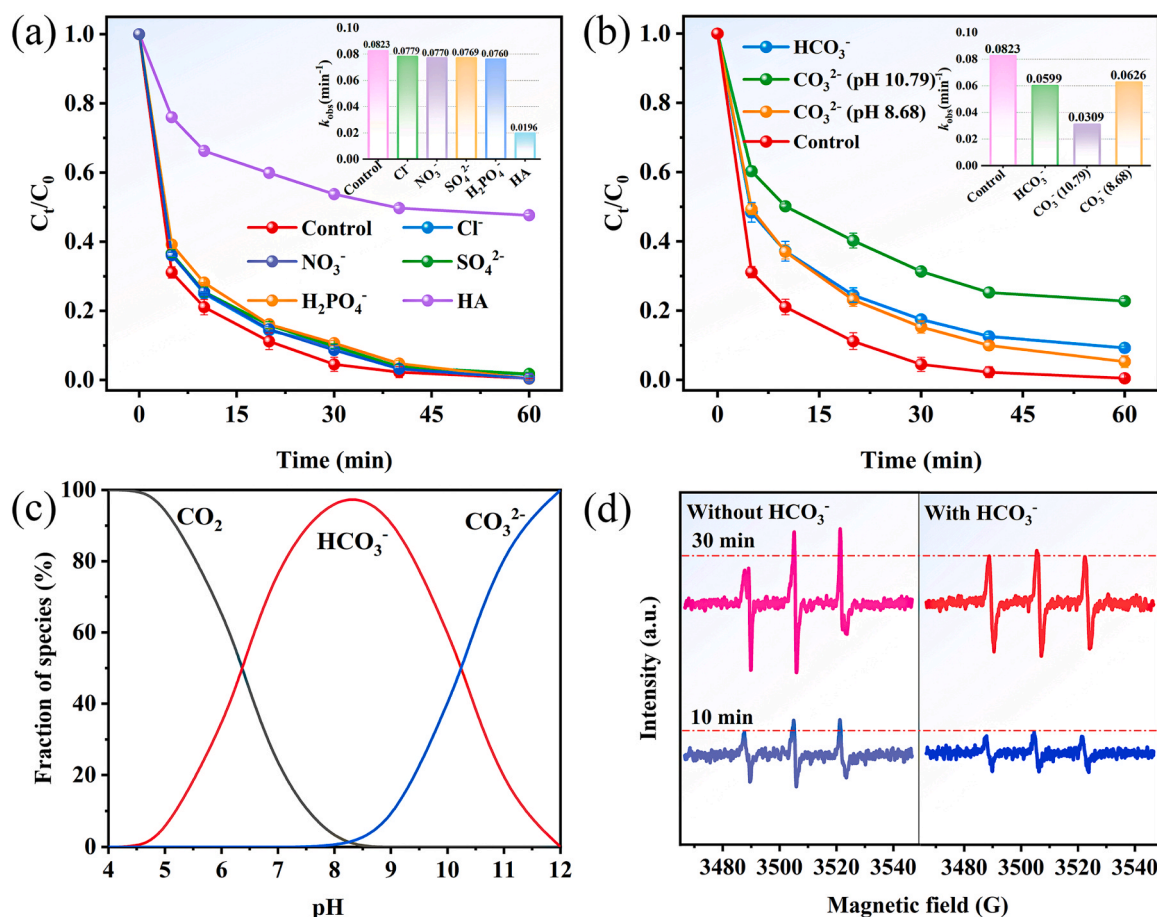


Fig. 9. (a) Effect of anions (Cl^- , SO_4^{2-} , NO_3^- , and H_2PO_4^-) and humic acid; (b) Effect of HCO_3^- and CO_3^{2-} under different pH condition; (c) The distribution of HCO_3^- and CO_3^{2-} at various pH conditions; (d) EPR spectra of with and without HCO_3^- . Reaction conditions: [BPA] = 20 mg L⁻¹, [PS] = 0.5 mM, [CF-1.0] = 0.3 g L⁻¹, [Anions] = 10 mM, [HA] = 0.2 g L⁻¹, [TEMP] = 50 mM, initial solution pH = 6.34, unless especially highlighted in the figure.

(Fig. S21a). Related water quality parameters were generalized in Table S7. The BPA concentrations in tap and lake water were both 20 mg L⁻¹, and the removal rates were as high as 94.4% and 86.9%, respectively. Even in 0.2 mg L⁻¹ and 0.5 mg L⁻¹ landfill leachate, the removal was still preserved at 77.7% and 80.8%, respectively, exhibiting the potential applications for wastewater remediation. Apart from BPA, the CF-1.0/PS system obtained impressive degradation performance towards sulfamethoxazole (SMX), sulfamonomethoxine (SMM), and rhodamine B (Rh-B), as described by the removal rate of more than 84.3% (Fig. S21b).

3.6. Effects of other oxidants and periodate activation mechanism

Notably, replacing PS with PMS lowered BPA oxidation rate from 99.5% to 91.0% (Fig. S22a). This was attributed to that the oxidation capacity of carbon-activated PMS (C-HSO_5^*) was smaller than the activated PS ($\text{C-S}_2\text{O}_8^{2*}$) in electron-transfer regime, given the lower intrinsic oxidation potential of PMS (1.75 V) instead of PS (2.01 V). Of particular, one achieved 70.0% removal rate when periodate (PI) was employed as the oxidant. In recent, PI-based advanced oxidation processes (PI-AOPs) has become a research hotspot by virtue of multiple reactive species, including IO_3^- , $\cdot\text{OH}$, $\text{O}_2^{\cdot-}$, and $^1\text{O}_2$ [48]. He et al. found that Fe₃N-doped carbonaceous catalysts could activate PI and degrade sulfadiazine via electron transfer [49]. Herein, the electron transfer pathway was identified by utilizing LSV. Clearly, the response current increased from 0.62 mA to 0.98 mA when PI and BPA were added simultaneously, implying the occurrence of the electron transfer pathway in the CF-1.0/PI/BPA system (Fig. S22b). Furthermore, the degradation

inhibition of 25.0% after adding NaClO_4 also supported our speculation. As could be seen the EPR spectra in Fig. S22c-d, the characteristic signals of $\text{DMPO}\cdot\text{OH}$, $\text{DMPO}\cdot\text{O}_2^{\cdot-}$, and $\text{TEMP}\cdot^1\text{O}_2$ proved the involvement of $\cdot\text{OH}$, $\text{O}_2^{\cdot-}$, and $^1\text{O}_2$. Furthermore, the active sites and possible activation mechanism of PI on CF-1.0 was proposed (Text S13 and Fig. S23).

3.7. Degradation pathways and intermediates identification

The BPA degradation intermediates were identified by liquid chromatography-mass spectrometry (LC-MS) (Fig. 10). Table S8 summarized the eight possible intermediates, and the relevant MS and MS² spectra were shown in Fig. S24. In pathway A, the hydroxylation reaction happened on the aromatic ring and converted into mono-hydroxylated intermediate P1 ($m/z = 243.10258$ [M-H]⁻) [50]. In P1, the newly introduced hydroxyl group enhanced the electron cloud density of phenyl ring, thereby, the catechol analogues were easily oxidized by $^1\text{O}_2$ to produce *ortho*-benzoquinone derivative P2 ($m/z = 241.08713$ [M-H]⁻) (pathway B) [3]. In pathway C, the two-molecule BPA intermediate P3 ($m/z = 453.20779$ [M-H]⁻) was as a result of BPA- O^\cdot radical dimerization, wherein BPA- O^\cdot was generated by the reaction of BPA with $\text{SO}_4^{\cdot-}/\cdot\text{OH}$ [51]. For pathway D, 4-(2-hydroxypropan-2-yl) phenol P4 ($m/z = 151.07642$ [M-H]⁻) was derived from the β -scission and subsequent hydroxylation of allyl carbon atom on BPA [3]. As for P4, a further nucleophilic attack by $\cdot\text{OH}$ on the phenol ring yielded P5 ($m/z = 167.07137$ [M-H]⁻) (pathway E1). In pathway E2, 4-methylbenzoic acid P6 ($m/z = 135.04507$ [M-H]⁻) was formed by reductive dehydrocarbon and successive oxidation [52]. Similarly, in pathways F and G, P7 ($m/z = 133.06584$ [M-H]⁻) was achieved through

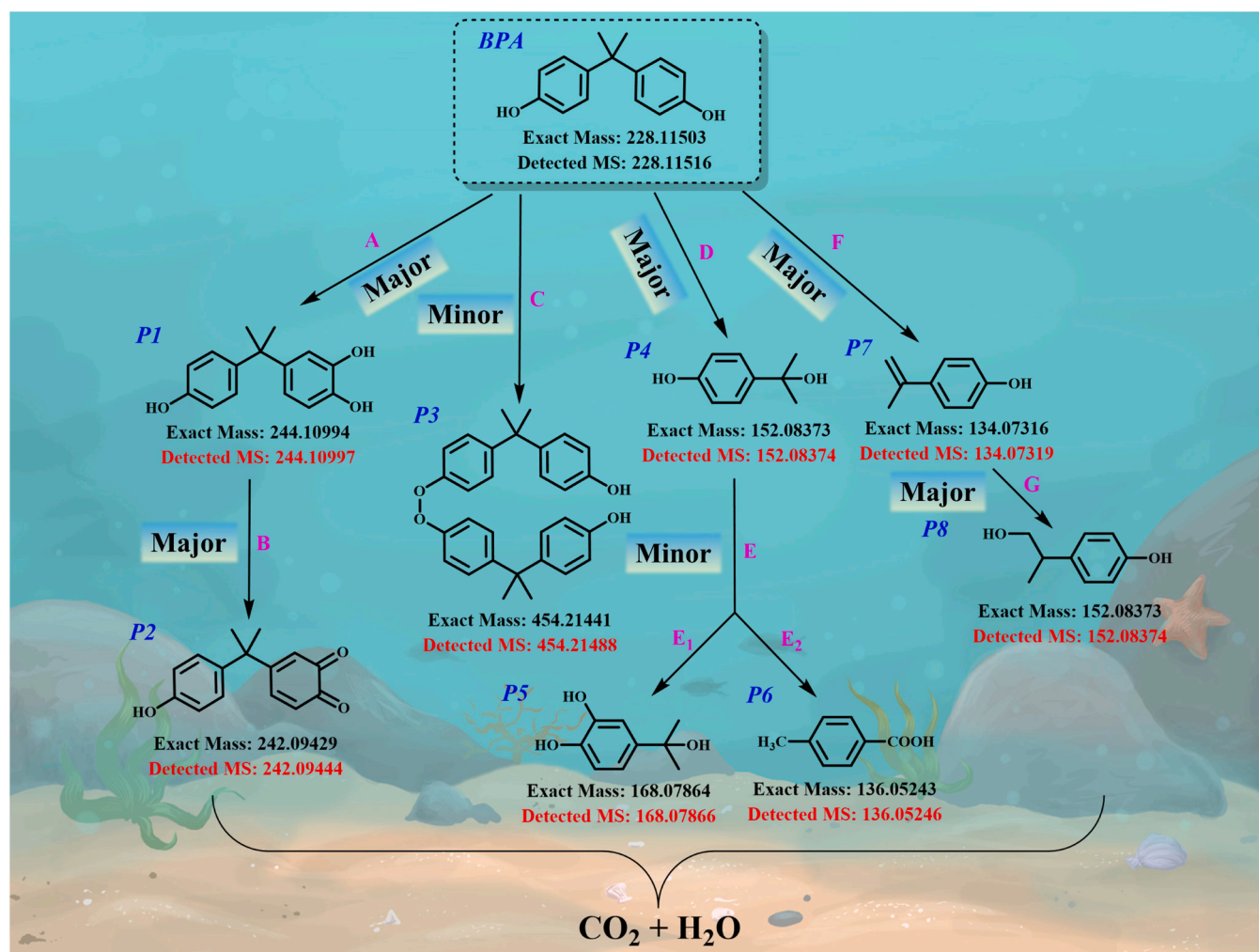


Fig. 10. The plausible degradation pathways of BPA.

β -break and electron rearrangement, followed by nucleophilic addition of vinyl and $\cdot\text{OH}$ to produce P8 ($m/z = 151.07642 [\text{M}-\text{H}]^-$) [4]. Based on the relative intensity of intermediates in LC-MS (Table S9), three main degradation pathways were ascertained including BPA \rightarrow A \rightarrow B, BPA \rightarrow D, and BPA \rightarrow F \rightarrow G, implying that a domination of hydroxylation reaction and β -break. Finally, these products from various pathways underwent deep oxidation to form H₂O and CO₂. Moreover, the data of total organic carbon (TOC) about 82.3% supported the efficient mineralization of BPA in the CF-1.0/PS system (Fig. S25).

4. Conclusion

In summary, F-doped carbonaceous persulfate activator was successfully synthesized through hydrothermal treatment with glucose/polytetrafluoroethylene dispersion and the subsequent high temperature carbonization. The incorporation of F atom not only improved the catalytic properties, but also caused the oxidation mechanism transformation from radical to electron transfer process. The as-synthesized CF-1.0 exhibited the best performance, corresponding to 99.5% BPA removal rate and 82.3% mineralization. The reaction rate constant was as high as 0.0823 min^{-1} . Quantitative structure-activity relationships (QSARs) indicated that semi-ionic C-F, C-OH, and structural defects function as electron transfer channel, $\text{SO}_4^{\cdot-}/\cdot\text{OH}$, and $^1\text{O}_2$ formation sites, respectively. Seven possible degradation pathways have been proposed. This research provides a feasible approach for the rational design of reaction-targeted carbocatalysts for persulfate activation.

More importantly, it sheds new light on the critical role of positively charged carbon in electron-transfer regime.

CRediT authorship contribution statement

Feng Ye: Writing – original draft, Formal analysis, Validation, Data curation. **Yinmei Su:** Investigation, Validation. **Ruipeng Li:** Investigation, Validation. **Wei Sun:** Writing-Modification, Conceptualization, Methodology. **Mengjie Pu:** Resources. **Cao Yang:** Resources. **Wenchao Yang:** Resources. **Haiming Huang:** Writing – review & editing. **Qichun Zhang:** Writing – review & editing. **Jonathan W.C. Wong:** Writing-Modification, Conceptualization, Methodology.

Declaration of Competing Interest

The authors declare that they have no known competing financial interests or personal relationships that could have appeared to influence the work reported in this paper.

Data Availability

Data will be made available on request.

Acknowledgments

This study was financially supported by the GuangDong Basic and

Applied Basic Research Foundation (No. 2019A1515110649; 2020A1515110271; 2019A1515110244), the Guangdong Province Universities and Colleges Pearl River Scholar Funded Scheme (2017), the Research Team in Dongguan University of Technology (No. TDYB2019013).

Appendix A. Supporting information

Supplementary data associated with this article can be found in the online version at [doi:10.1016/j.apcatb.2023.122992](https://doi.org/10.1016/j.apcatb.2023.122992).

References

- X. Sun, M. Xie, L. Mai, E.Y. Zeng, Biobased plastic: a plausible solution toward carbon neutrality in plastic industry, *J. Hazard. Mater.* 435 (2022), 129037, <https://doi.org/10.1016/j.jhazmat.2022.129037>.
- W. Chen, D. He, J. Huang, K. Zhu, L. Lei, H. He, Y. Ai, One-step synthesis of novel Fe/Fe₃O₄ embedded in N-doped graphite-like carbon nanosheets with the entangled CNTs to activate peroxymonosulfate for bisphenol A degradation, *Sep. Purif. Technol.* 295 (2022), 121172, <https://doi.org/10.1016/j.seppur.2022.121172>.
- Y. Wang, L. Wang, F. Ma, Y. You, FeO_x@graphitic carbon core-shell embedded in microporous N-doped biochar activated peroxydisulfate for removal of Bisphenol A: Multiple active sites induced non-radical/radical mechanism, *Chem. Eng. J.* 438 (2022), 135552, <https://doi.org/10.1016/j.cej.2022.135552>.
- Y. He, C. He, L. Lai, P. Zhou, H. Zhang, L. Li, Z. Xiong, Y. Mu, Z. Pan, G. Yao, B. Lai, Activating peroxymonosulfate by N and O co-doped porous carbon for efficient BPA degradation: a re-visit to the removal mechanism and the effects of surface unpaired electrons, *Appl. Catal. B: Environ.* 314 (2022), 121390, <https://doi.org/10.1016/j.apcatb.2022.121390>.
- G. Cao, Q. Li, R. Wang, C. Wang, X. Duan, S.H. Ho, Simultaneous separation of multiphase emulsion mixture and catalytic degradation of BPA via microalgae residue membranes, *Chem. Eng. J.* 393 (2020), 124750, <https://doi.org/10.1016/j.cej.2020.124750>.
- M. Rani, U. Rachna, Shanker, Efficient photocatalytic degradation of Bisphenol A by metal ferrites nanoparticles under sunlight, *Environ. Technol. Inno* 19 (2020), 100792, <https://doi.org/10.1016/j.eti.2020.100792>.
- Z. Sun, L. Zhao, C. Liu, Y. Zhen, J. Ma, Fast adsorption of BPA with high capacity based on π - π electron donor-acceptor and hydrophobicity mechanism using an in-situ sp² C dominant N-doped carbon, *Chem. Eng. J.* 381 (2020), 122510, <https://doi.org/10.1016/j.cej.2019.122510>.
- X. Chen, D. Vione, T. Borch, J. Wang, Y. Gao, Nano-MoO₂ activates peroxymonosulfate for the degradation of PAH derivatives, *Water Res* 192 (2021), 116834, <https://doi.org/10.1016/j.watres.2021.116834>.
- H. Luo, Y. Wan, H. Zhou, Y. Cai, M. Zhu, Z. Dang, H. Yin, Mechanisms and influencing factors for electron transfer complex in metal-biochar nanocomposites activated peroxydisulfate, *J. Hazard. Mater.* 438 (2022), 129461, <https://doi.org/10.1016/j.jhazmat.2022.129461>.
- J. Yu, H. Feng, L. Tang, Y. Pang, G. Zeng, Y. Lu, H. Dong, J. Wang, Y. Liu, C. Feng, J. Wang, B. Peng, S. Ye, Metal-free carbon materials for persulfate-based advanced oxidation process: Microstructure, property and tailoring, *Prog. Mater. Sci.* 111 (2020), 100654, <https://doi.org/10.1016/j.pmatsci.2020.100654>.
- W. Huang, S. Xiao, H. Zhong, M. Yan, X. Yang, Activation of persulfates by carbonaceous materials: a review, *Chem. Eng. J.* 418 (2021), 129297, <https://doi.org/10.1016/j.cej.2021.129297>.
- Y. Qi, B. Ge, Y. Zhang, B. Jiang, C. Wang, M. Akram, X. Xu, Three-dimensional porous graphene-like biochar derived from Enteromorpha as a persulfate activator for sulfamethoxazole degradation: Role of graphitic N and radicals transformation, *J. Hazard. Mater.* 399 (2020), 123039, <https://doi.org/10.1016/j.jhazmat.2020.123039>.
- W. Duan, J. He, Z. Wei, Z. Dai, C. Feng, A unique Si-doped carbon nanocatalyst for peroxymonosulfate (PMS) activation: insights into the singlet oxygen generation mechanism and the abnormal salt effect, *Environ. Sci. Nano* 7 (2020) 2982–2994, <https://doi.org/10.1039/D0EN00848F>.
- B. Liu, W. Guo, H. Wang, Q. Si, Q. Zhao, H. Luo, N. Ren, B-Doped graphitic porous biochar with enhanced surface affinity and electron transfer for efficient peroxydisulfate activation, *Chem. Eng. J.* 396 (2020), 125119, <https://doi.org/10.1016/j.cej.2020.125119>.
- M. Cheng, R. Ma, G. Chai, Y. Chen, L. Bai, D. Wang, J. Qian, G. Chen, Nitrogen-doped carbonized polyaniline (N-CPANI) for peroxydisulfate (PDS) activation towards efficient degradation of doxycycline (DOX) via the non-radical pathway dominated by electron transfer, *Chem. Eng. J.* 453 (2023), 139810, <https://doi.org/10.1016/j.cej.2022.139810>.
- W. Ren, G. Nie, P. Zhou, H. Zhang, X. Duan, S. Wang, The intrinsic nature of persulfate activation and N-doping in carbocatalysis, *Environ. Sci. Technol.* 54 (2020) 6438–6447, <https://doi.org/10.1021/acs.est.0c01161>.
- H. Wang, W. Guo, B. Liu, Q. Wu, H. Luo, Q. Zhao, Q. Si, F. Sseguya, N. Ren, Edge-nitrogenated biochar for efficient peroxydisulfate activation: An electron transfer mechanism, *Water Res* 160 (2019) 405–414, <https://doi.org/10.1016/j.watres.2019.05.059>.
- J. Kang, X. Duan, L. Zhou, H. Sun, M.O. Tadé, S. Wang, Carbocatalytic activation of persulfate for removal of antibiotics in water solutions, *Chem. Eng. J.* 288 (2016) 399–405, <https://doi.org/10.1016/j.cej.2015.12.040>.
- W. Ma, Y. Du, N. Wang, P. Miao, ZIF-8 derived nitrogen-doped porous carbon as metal-free catalyst of peroxymonosulfate activation, *Environ. Sci. Pollut. R.* 24 (2017) 16276–16288, <https://doi.org/10.1007/s11356-017-9191-2>.
- X. Chen, X. Duan, W. Oh, P. Zhang, C. Guan, Y. Zhu, T.T. Lim, Insights into nitrogen and boron-co-doped graphene toward high-performance peroxymonosulfate activation: maneuverable N-B bonding configurations and oxidation pathways, *Appl. Catal. B: Environ.* 253 (2019) 419–432, <https://doi.org/10.1016/j.apcatb.2019.04.018>.
- J. Dou, J. Cheng, Z. Lu, Z. Tian, J. Xu, Y. He, Biochar co-doped with nitrogen and boron switching the free radical based peroxydisulfate activation into the electron-transfer dominated nonradical process, *Appl. Catal. B: Environ.* 301 (2022), 120832, <https://doi.org/10.1016/j.apcatb.2021.120832>.
- G. Wang, Y. Liu, X. Dong, X. Zhang, Transforming radical to non-radical pathway in peroxymonosulfate activation on nitrogen doped carbon sphere for enhanced removal of organic pollutants: combined effect of nitrogen species and carbon structure, *J. Hazard. Mater.* 437 (2022), 129357, <https://doi.org/10.1016/j.jhazmat.2022.129357>.
- S. Ye, G. Zeng, X. Tan, H. Wu, J. Liang, B. Song, N. Tang, P. Zhang, Y. Yang, Q. Chen, X. Li, Nitrogen-doped biochar fiber with graphitization from Boehmeria nivea for promoted peroxymonosulfate activation and non-radical degradation pathways with enhancing electron transfer, *Appl. Catal. B: Environ.* 269 (2020), 118850, <https://doi.org/10.1016/j.apcatb.2020.118850>.
- C. Fu, G. Sun, G. Yin, C. Wang, G. Ran, Q. Song, P/N Co-doped carbon sheet for peroxymonosulfate activation: edge sites enhanced adsorption and subsequent electron transfer, *Sep. Purif. Technol.* 292 (2022), 120922, <https://doi.org/10.1016/j.seppur.2022.120922>.
- F. Ye, Y. Shi, W. Sun, K. Pang, M. Pu, L. Yang, H. Huang, Construction of adsorption-oxidation bifunction-oriented carbon by single boron doping for non-radical antibiotic degradation via persulfate activation, *Chem. Eng. J.* 454 (2023), 140148, <https://doi.org/10.1016/j.cej.2022.140148>.
- K. Zhang, X. Min, T. Zhang, M. Xie, M. Si, L. Chai, Y. Shi, Selenium and nitrogen co-doped biochar as a new metal-free catalyst for adsorption of phenol and activation of peroxymonosulfate: Elucidating the enhanced catalytic performance and stability, *J. Hazard. Mater.* 413 (2021), 125294, <https://doi.org/10.1016/j.jhazmat.2021.125294>.
- R. Jiang, Q. Zhi, W. Liu, Z. Gao, X. Zhan, Y. Jin, K. Wang, T. Sun, W. Li, J. Jiang, F-Doped carbon hollow nanospheres for efficient electrochemical oxygen reduction, *J. Mater. Sci.* 57 (2022) 5924–5932, <https://doi.org/10.1007/s10853-022-06972-9>.
- W. Xie, J. Huang, L. Huang, S. Geng, S. Song, P. Tsiakaras, Y. Wang, Novel fluorine-doped cobalt molybdate nanosheets with enriched oxygen-vacancies for improved oxygen evolution reaction activity, *Appl. Catal. B: Environ.* 303 (2022), 120871, <https://doi.org/10.1016/j.apcatb.2021.120871>.
- S. Liu, C. Lai, X. Zhou, C. Zhang, L. Chen, H. Yan, L. Qin, D. Huang, H. Ye, W. Chen, L. Li, M. Zhang, L. Tang, F. Xu, D. Ma, Peroxydisulfate activation by sulfur-doped ordered mesoporous carbon: Insight into the intrinsic relationship between defects and ¹O₂ generation, *Water Res* 221 (2022), 118797, <https://doi.org/10.1016/j.watres.2022.118797>.
- Y. Liu, Q. Li, X. Guo, X. Kong, J. Ke, M. Chi, Q. Li, Z. Geng, J. Zeng, A highly efficient metal-free electrocatalyst of F-doped porous carbon toward N₂ electroreduction, *Adv. Mater.* 32 (2020) 1907690, <https://doi.org/10.1002/adma.201907690>.
- T. Wang, X. Zhang, X. Wang, X. Gu, Q. Shao, N. Cao, Recent advances in fluorine-doped/fluorinated carbon-based materials for supercapacitors, *Energy Storage Mater.* 30 (2020) 367–384, <https://doi.org/10.1016/j.ensm.2020.04.044>.
- D. Liu, J. Wang, Z. Li, Z. Yun, Y. Zhang, J. Huang, Ultrathin nitrogen-rich porous carbon nanosheets with fluorine doping for high-performance potassium storage, *Electrochim. Acta* 411 (2022), 140094, <https://doi.org/10.1016/j.electacta.2022.140094>.
- C. Buttersack, Modeling of type IV and V sigmoidal adsorption isotherms, *Phys. Chem. Chem. Phys.* 21 (2019) 5614–5626, <https://doi.org/10.1039/C8CP07751G>.
- D. Yuan, Z. Wei, P. Han, C. Yang, L. Huang, Z. Gu, Y. Ding, J. Ma, G. Zheng, Electron distribution tuning of fluorine-doped carbon for ammonia electrosynthesis, *J. Mater. Chem. A* 7 (2019) 16979–16983, <https://doi.org/10.1039/C9TA04141A>.
- T. Zhu, S. Liu, K. Wan, C. Zhang, Y. Feng, W. Feng, T. Liu, Fluorine and nitrogen dual-doped porous carbon nanosheet-enabled compact electrode structure for high volumetric energy storage, *ACS Appl. Mater. Sci.* 3 (2020) 4949–4957, <https://doi.org/10.1021/acsaem.0c00500>.
- Y. Long, S. Li, P. Yang, X. Chen, W. Liu, X. Zhan, C. Xue, D. Liu, W. Huang, Synthesis of ZIF-67 derived honeycomb porous Co/NC catalyst for AO₂ degradation via activation of peroxymonosulfate, *Sep. Purif. Technol.* 286 (2022), 120470, <https://doi.org/10.1016/j.seppur.2022.120470>.
- A. Ait El Fakir, Z. Anfar, M. Enneimy, A. Jada, N. El Alem, Conjugated polymers templated carbonization to design N,S co-doped finely tunable carbon for enhanced synergistic catalysis, *Appl. Catal. B: Environ.* 300 (2022), 120732, <https://doi.org/10.1016/j.apcatb.2021.120732>.
- X. Li, Y. Jia, M. Zhou, X. Su, J. Sun, High-efficiency degradation of organic pollutants with Fe,N co-doped biochar catalysts via persulfate activation, *J. Hazard. Mater.* 397 (2020), 122764, <https://doi.org/10.1016/j.jhazmat.2020.122764>.
- H. Qiu, P. Guo, L. Yuan, G. Sheng, Different non-radical oxidation processes of persulfate and peroxymonosulfate activation by nitrogen-doped mesoporous

- carbon, *Chin. Chem. Lett.* 31 (2020) 2614–2618, <https://doi.org/10.1016/j.cclet.2020.08.014>.
- [40] X. Pan, J. Chen, N. Wu, Y. Qi, X. Xu, J. Ge, X. Wang, C. Li, R. Qu, V.K. Sharma, Z. Wang, Degradation of aqueous 2,4,4'-trihydroxybenzophenone by persulfate activated with nitrogen doped carbonaceous materials and the formation of dimer products, *Water Res* 143 (2018) 176–187, <https://doi.org/10.1016/j.watres.2018.06.038>.
- [41] W. Ren, C. Cheng, P. Shao, X. Luo, H. Zhang, S. Wang, X. Duan, Origins of electron-transfer regime in persulfate-based nonradical oxidation processes, *Environ. Sci. Technol.* 56 (2022) 78–97, <https://doi.org/10.1021/acs.est.1c05374>.
- [42] Q. Yang, Y. Chen, X. Duan, S. Zhou, Y. Niu, H. Sun, L. Zhi, S. Wang, Unzipping carbon nanotubes to nanoribbons for revealing the mechanism of nonradical oxidation by carbocatalysis, *Appl. Catal. B: Environ.* 276 (2020), 119146, <https://doi.org/10.1016/j.apcatb.2020.119146>.
- [43] W. Ren, L. Xiong, G. Nie, H. Zhang, X. Duan, S. Wang, Insights into the electron-transfer regime of peroxydisulfate activation on carbon nanotubes: The role of oxygen functional groups, *Environ. Sci. Technol.* 54 (2020) 1267–1275, <https://doi.org/10.1021/acs.est.9b06208>.
- [44] J. Yan, W. Gao, M. Dong, L. Han, L. Qian, C.P. Nathanail, M. Chen, Degradation of trichloroethylene by activated persulfate using a reduced graphene oxide supported magnetite nanoparticle, *Chem. Eng. J.* 295 (2016) 309–316, <https://doi.org/10.1016/j.cej.2016.01.085>.
- [45] X. Cheng, H. Guo, Y. Zhang, G.V. Korshin, B. Yang, Insights into the mechanism of nonradical reactions of persulfate activated by carbon nanotubes: Activation performance and structure-function relationship, *Water Res* 157 (2019) 406–414, <https://doi.org/10.1016/j.watres.2019.03.096>.
- [46] O.S. Furman, A.L. Teel, R.J. Watts, Mechanism of base activation of persulfate, *Environ. Sci. Technol.* 44 (2010) 6423–6428, <https://doi.org/10.1021/es1013714>.
- [47] X. Huo, P. Zhou, J. Zhang, Y. Liu, X. Cheng, Y. Liu, W. Li, Y. Zhang, N. S-Doped, porous carbons for persulfate activation to remove tetracycline: nonradical, *Mech. J. Hazard. Mater.* 391 (2020), 122055, <https://doi.org/10.1016/j.jhazmat.2020.122055>.
- [48] C. Ling, S. Wu, J. Han, T. Dong, C. Zhu, X. Li, L. Xu, Y. Zhang, M. Zhou, Y. Pan, Sulfide-modified zero-valent iron activated periodate for sulfadiazine removal: performance and dominant routine of reactive species production, *Water Res* 220 (2022), 118676, <https://doi.org/10.1016/j.watres.2022.118676>.
- [49] L. He, C. Yang, J. Ding, M. Lu, C. Chen, G. Wang, J. Jiang, L. Ding, G. Liu, N. Ren, S. Yang, Fe,N-doped carbonaceous catalyst activating periodate for micropollutant removal: significant role of electron transfer, *Appl. Catal. B: Environ.* 303 (2022), 120880, <https://doi.org/10.1016/j.apcatb.2021.120880>.
- [50] Y. Sun, J. Yu, X. Zhan, L. Chen, Y. Zhao, H. Wang, H. Shi, A copper-loaded N-doped carbon catalyst with mesoporous hollow sphere structure for bisphenol A removing via peroxymonosulfate activation, *Micro Mesopor. Mat.* 342 (2022), 112133, <https://doi.org/10.1016/j.micromeso.2022.112133>.
- [51] Y. Wang, Y. Lin, C. Yang, S. Wu, X. Fu, X. Li, Calcination temperature regulates non-radical pathways of peroxymonosulfate activation via carbon catalysts doped by iron and nitrogen, *Chem. Eng. J.* 451 (2023), 138468, <https://doi.org/10.1016/j.cej.2022.138468>.
- [52] S. Wang, J. Tian, Q. Wang, F. Xiao, S. Gao, W. Shi, F. Cui, Development of CuO coated ceramic hollow fiber membrane for peroxymonosulfate activation: a highly efficient singlet oxygen-dominated oxidation process for bisphenol A degradation, *Appl. Catal. B: Environ.* 256 (2019), 117783, <https://doi.org/10.1016/j.apcatb.2019.117783>.